

Antarctic Intermediate Water Circulation and Variability in a Coupled Climate Model

AGUS SANTOSO AND MATTHEW H. ENGLAND

*Centre for Environmental Modelling and Prediction, School of Mathematics, University of New South Wales, Sydney,
New South Wales, Australia*

(Manuscript received 22 October 2002, in final form 19 April 2004)

ABSTRACT

The variability of Antarctic Intermediate Water (AAIW) in a long-term natural integration of a coupled climate model is examined. The mean state of the climate model includes a realistic representation of AAIW, which appears centered on the $\sigma_\theta = 27.2 \text{ kg m}^{-3}$ density surface (hereinafter $\sigma_{27.2}$) both in observations and the model. An assessment of ventilation rates on the $\sigma_{27.2}$ surface suggests that this particular climate model forms AAIW in a mostly circumpolar fashion, with a significant contribution from Antarctic Surface Water. This motivates the assessment of oceanic variability along this core AAIW isopycnal surface. Complex empirical orthogonal function analyses decompose the variability into three dominant modes showing circumpolar patterns of zonal wavenumber-1, -2, and -3 on the $\sigma_{27.2}$ density surface. The modes contain eastward-propagating signals at interannual to centennial time scales. Mechanisms forcing this variability are investigated using heat and salt budget analyses at the wintertime outcrop of the $\sigma_{27.2}$ surface. Such an approach ignores the mechanism of AAIW variability sourced by Subantarctic Mode Water variations, which has been examined previously and is, for the most part, beyond the present study. Variability in meltwater rates and atmospheric heat and freshwater fluxes are found to dominate the intermediate water variability at the outcrop region. In contrast, northward Ekman transport of heat and salt plays a significant but localized role in AAIW temperature–salinity variability. There is also an important contribution from the Antarctic Circumpolar Current to the variability at the outcrop region via zonal transport of heat and salt. While the magnitude of AAIW natural variability can be large near the outcrop of the salinity minimum layer, recent observations of cooling and freshening at depth are suggested to be beyond that of the unperturbed system.

1. Introduction

The increasing number of studies on Antarctic Intermediate Water (AAIW) formation and variability (e.g., Piola and Georgi 1982; England 1992; England et al. 1993; Johnson and Orsi 1997; Wong et al. 1999; Arbic and Owens 2001; Sørensen et al. 2001; Saenko et al. 2003) reflects the importance of this water mass in balancing the global-scale oceanic heat and salt transport. Understanding and quantifying natural variability of AAIW is crucial to an understanding of longer-term climate change. In particular, the detection and attribution of climate change at intermediate layers of the Southern Ocean depend on a knowledge of the magnitude and dynamics of AAIW variability. The goal of this study is to quantify and explain interannual- to centennial-scale variability of AAIW using a coupled climate model.

AAIW is found in all sectors of the Southern Hemisphere oceans to the north of the Antarctic polar front (APF). AAIW temperature–salinity properties and cir-

culatation have already been documented in many studies based on observational data (e.g., Deacon 1933; Georgi 1979; Piola and Georgi 1982). Depending on the location in the ocean, AAIW has generally been characterized as a salinity minimum water mass in the Antarctic polar front zone (APFZ) with a typical salinity of 34.2–34.4 psu and temperature of 3°–5°C (e.g., Georgi 1979; Piola and Georgi 1982). AAIW spreads northward to intermediate depths of approximately 800–1000 m at 40°S and is found as far north as 30°N in the North Atlantic Ocean (e.g., Pickard and Emery 1990; Talley 1996). As it flows northward from the source region, its salinity increases as it mixes with more saline water from above and below. The density surfaces associated with the core of AAIW fall in the range 1027.2–1027.3 kg m^{-3} (e.g., Molinelli 1981; Piola and Georgi 1982) and shoal south of the APF (refer to Molinelli 1981, his Fig. 11).

The formation process of AAIW has long been an area of research resulting in a variety of mechanisms still under debate. As first described by Wüst (1935), AAIW is identified in the Southern Ocean by a salinity minimum layer that descends near the APFZ. Sverdrup et al. (1942) proposed that AAIW is formed by circumpolar subduction or along-isopycnal transport along the

Corresponding author address: Matthew England, School of Mathematics, University of New South Wales, Sydney, NSW 2052, Australia.
E-mail: M.England@unsw.edu.au

APFZ, supported by the circumpolar presence of AAIW. In contrast, McCartney (1977) suggested that AAIW is primarily a by-product of Subantarctic Mode Water (SAMW), formed in a deep convective mixed layer in the southeast Pacific Ocean off southern Chile, feeding into the Pacific Ocean and via the Drake Passage to the southwest Atlantic. Molinelli (1981), on the other hand, suggested that isopycnal processes, both mixing and geostrophic flow, dominate AAIW formation along the APFZ, with Antarctic Surface Water (AASW) mixing with waters at depth in the subantarctic zone. In addition, Molinelli (1981) found significant input of AASW along the $\sigma_\theta = 27.2\text{--}27.3 \text{ kg m}^{-3}$ isopycnal layer in the southeast Pacific and near Kerguelen Island (80°E). Other studies based on observational data support one or a combination of McCartney's (1977) and Molinelli's (1981) suggestions on AAIW formation in the southeast Pacific and southwest Atlantic (e.g., Georgi 1979; Piola and Georgi 1982; Piola and Gordon 1989; Talley 1996). A recent study by Sloyan and Rintoul (2001) found that cross-frontal exchange of AASW to SAMW together with deep winter mixing, dominate the renewal of AAIW via diapycnal exchange. This is in contrast to the along-isopycnal process proposed by Molinelli (1981). In short, mechanisms of AAIW renewal are still under vigorous debate.

Model simulations of AAIW have improved with the evolution of prognostic z -coordinate ocean general circulation models. England (1992) was the first to capture a salinity minimum in the Southern Ocean in a coarse-resolution model, although his AAIW was too saline and lacked the northward penetration observed. This could be attributed to the unphysical treatment of horizontal mixing in these earlier ocean models. Some improvement was realized upon the inclusion of the Redi (1982) mixing scheme for along-isopycnal diffusion (England 1993), with the AAIW formation mechanism largely consistent with McCartney's (1977) view (England et al. 1993). Further improvement in AAIW representation can be achieved upon the inclusion of the Gent and McWilliams (1990) parameterization (GM) for adiabatic transport of tracers by eddies (e.g., Hirst and McDougall 1996; Large et al. 1997; Duffy and Caldeira 1997; Duffy et al. 1999; Sørensen et al. 2001), although not all such models attain realistic AAIW temperature–salinity. In GM models it appears that AASW plays a more significant role in AAIW formation along the APFZ, including the model used in this study, as a result of reduced midlatitude to subpolar convection in the Southern Ocean (e.g., Sørensen et al. 2001).

The model sensitivity of AAIW to choice of surface forcing has also been studied (e.g., England 1993; Hirst and McDougall 1996; Duffy et al. 1999). However, only recently has the effect of freshwater forcing due to Antarctic sea ice been shown to be important (Duffy et al. 2001; Saenko and Weaver 2001). Using a coupled ocean–ice model, Saenko and Weaver (2001) showed that high-latitude westerlies at the Antarctic sea-ice mar-

gin induce northward Ekman transport of sea ice where it melts and feeds freshwater in the regions where AAIW isopycnal surfaces outcrop. Furthermore, using the same model Saenko et al. (2003) found nonuniform subduction of AAIW and a localized northward flux of freshwater in the southeast Pacific. This is in contrast to the 2D circumpolar view of AAIW formation found by Sørensen et al. (2001), though the Sørensen et al. (2001) study ignores sea-ice effects in an uncoupled configuration.

Spatial variations in the temperature and salt (T – S) properties of AAIW are detected in different locations of the Southern Ocean. For example, a study conducted by Piola and Georgi (1982) based on observational data documents the circumpolar properties of AAIW in the latitude band $40^\circ\text{--}45^\circ\text{S}$. They found different varieties of AAIW in each of the three ocean basins. The Indian Ocean AAIW is warmer and saltier than in the South Atlantic while AAIW salinity decreases abruptly east of 160°W where the South Pacific variety of AAIW is found. Furthermore, Piola and Georgi (1982) found that large changes in the properties of AAIW occur in the transition regions between the three ocean basins.

Because of the sparsity of observational data, only a few studies of temporal changes in AAIW have been carried out. Bindoff and Church (1992) found a significant cooling of approximately $0.05^\circ\text{--}0.2^\circ\text{C}$ and freshening of $0.01\text{--}0.04 \text{ psu}$ (estimated from their Fig. 3) along density surfaces within 600–1000-m depth in the Tasman Sea at 43° and 28°S on the basis of measurements made 22 yr apart. Wong et al. (1999) found a basinwide freshening (zonally averaged decrease of 0.021 psu) along density surfaces of AAIW based on a 20-yr difference measured in the Pacific Ocean along 17°S . Based on the same measurements, Wong et al. (2001) found that the freshening and cooling along the density surfaces were also accompanied by freshening and cooling along isobars. They found that the T – S decrease extends southward to the subantarctic front along 150°W . Johnson and Orsi (1997) found mean cooling and freshening between 1968/69 and 1990 of approximately 0.1°C and 0.03 psu (estimated from their Fig. 5) along isopycnals associated with AAIW in the Pacific along 170°W from 48° to 20°S . Based on the methodology of Bindoff and McDougall (1994), Johnson and Orsi (1997) propose that the change is a result of surface freshening at high latitudes where isopycnals associated with AAIW outcrop before the water ventilates the base of the subtropical thermocline. Decadal changes in the Indian Ocean across 32°S between 1962 and 1987 have been documented by Wong et al. (1999) and Bindoff and McDougall (2000) with average cooling and freshening of 0.33°C and 0.06 psu along a neutral surface equivalent to the AAIW 1027.3 kg m^{-3} potential density surface. Arbic and Owens (2001) document an average warming of about 0.5°C (100 yr^{-1}) and a salinity increase of 0.1 psu (100 yr^{-1}) along isobars near 1000 dbar at 32° and 24°S in the southwestern Atlantic (see

their Figs. 3 and 4). They attributed the warming along the isobars, where AAIW is found, to watermass changes along isopycnal surfaces. Thus, variability in the ocean interior along isopycnals, where true watermass properties are defined, is attributable to variability at the region of watermass formation (e.g., Bindoff and Church 1992; Bindoff and McDougall 1994; Wong et al. 2001). Banks et al. (2000) compare the observed decadal changes, particularly for the Indian Ocean 32°S section, with the natural variability in a coupled climate model. They found weaker cooling and freshening than observed along intermediate water isopycnals in the 32°S section. Based on the weaker changes in the model, they suggest that the observed decadal changes in Bindoff and McDougall (2000) are likely to be a signal of anthropogenic climate change.

While the above studies have furthered our knowledge of natural and forced variations in AAIW at several isolated locations, there has been relatively little attention given to the mechanisms controlling watermass variability at intermediate depths. This is due in part to the sparsity and short period of observational data in the Southern Ocean. The goals of the present study are 1) to document the spatial and temporal variability of AAIW along isopycnal surfaces in a multicentury integration of a coupled atmosphere–ocean–ice model, 2) to evaluate the mechanisms controlling this variability by conducting heat/salt budget analyses at the late-winter outcrop locations of the isopycnal surfaces, and 3) to examine the patterns of propagation of these anomalies along isopycnals in space and time. We will address these three goals in sections 4 and 5. First, though, the coupled model and methods of analysis are described in section 2, and a brief description of the model simulated AAIW is provided in section 3. Last, we summarize the study in section 6.

2. The coupled model and methodology

a. The coupled model

The model used in this study is the Commonwealth Scientific and Industrial Research Organisation (CSIRO) 10 000-yr natural preindustrial CO₂ coupled ocean–atmosphere–ice–land surface model. This is an updated version of the 1000-yr coupled model employing the GM scheme as described in Hirst et al. (2000). The atmospheric model is discretized on nine levels in a sigma coordinate system. The model has full diurnal and annual cycles, gravity wave drag, a mass flux scheme for convection, semi-Lagrangian water vapor transport, and a relative humidity–based cloud parameterization (for details see Gordon and O’Farrell 1997; Hirst et al. 2000). The ocean model is based on the Bryan–Cox code (Cox 1984) employing GM and zero horizontal diffusivity. It has a resolution of approximately 3.2° latitude \times 5.6° longitude, with 21 vertical levels of irregular grid box thickness. The ocean model

resolution is typical of that used in previous studies of AAIW properties and dynamics (e.g., England et al. 1993; Sørensen et al. 2001). The atmospheric model is spectral with horizontal resolution limited by a rhomboidal truncation at wavenumber 21. A full description of the sea-ice model can be found in O’Farrell (1998). Advection and divergence of sea ice can result from both wind stress and motion by ocean currents.

We analyze 1000 yr of model data from the latter stages of the 10 000-yr run. It may be noted that the model exhibits minimal drift at this latter stage of the run. Variables analyzed include ocean potential temperature (denoted as θ hereinafter), salinity (S), and horizontal ocean velocities (u , v), as well as air–sea flux properties such as surface wind stress (τ^x , τ^y), and air–sea heat (Q), and salt (H) fluxes. Only data south of 20°S are considered in our analyses since the focus of this study is on the water masses of the Southern Ocean.

b. Diagnosis of AAIW variability

We divide this study into two parts. The first part is to document the variability of AAIW in the model. To this end, we analyze θ – S properties on the potential density surface $\rho_\theta = 1027.2 \text{ kg m}^{-3}$ (referred as $\sigma_{27.2}$ hereinafter). This density surface is chosen as it approximately coincides with both the model and observed intermediate water salinity minimum reaching depths of 700–1000 m to the north of 40°S (as can be seen in Fig. 1; discussed further in section 3). This potential density surface outcrops in winter near the maximum sea-ice margin in the model (Fig. 2a), as well as in the real ocean (Fig. 2b). In Fig. 2, discussed further in section 5, the observed θ – S data are based on the Levitus climatology (Levitus and Boyer 1994; Levitus et al. 1994) and the sea-ice-extent data are based on the monthly U.S. Navy–National Oceanic and Atmospheric Administration Joint Ice Center and passive microwave Defense Meteorological Satellite Program (DMSP) extending from January 1973 to September 1998.

It is of some interest to diagnose the relative ventilation rate along the chosen $\sigma_{27.2}$ AAIW density surface, in part to resolve where we should analyze model variability of this water mass. Figure 3 shows the $\sigma_{27.2}$ distribution of a passive tracer after 50 yr of release in the coupled climate model. The passive tracer is set to a value of 100% at the surface in the Southern Hemisphere for all time steps [and zero in the Northern Hemisphere surface layer; further details can be found in O’Farrell (2002)]. The passive tracer suggests an approximately zonally uniform distribution of AAIW ventilation over multidecadal time scales. The highest concentration of tracer occurs at the layer outcrop near 60°S, decreasing northward into the ocean interior along $\sigma_{27.2}$. The circumpolar penetration of passive tracer into the interior suggests Antarctic Surface Water (AASW) is the major source of AAIW formation in the model, both by direct subduction and indirectly via cross-front mix-

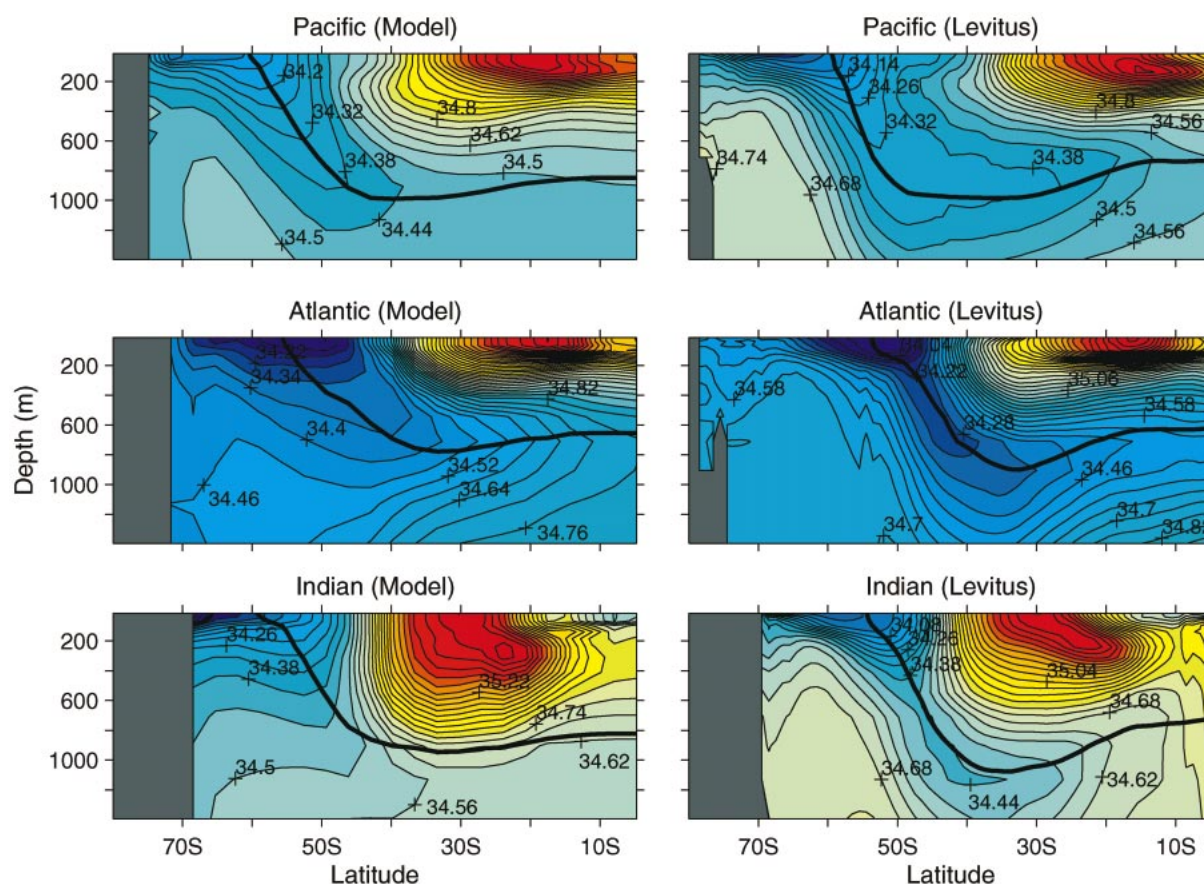


FIG. 1. Cross section of the zonally averaged late-winter salinity fields in the Pacific, Atlantic, and Indian sectors in the (left) model and (right) Levitus climatology. The thick line indicates the mean position of the $\sigma_{\theta} = 27.2 \text{ kg m}^{-3}$ isopycnal. Note that the same color scale is used for comparing the model and observed salinity for each ocean sector.

ing at the APFZ. Recycled mode water also contributes, with a slightly enhanced ventilation detected in the southeast Pacific Ocean, the Tasman Sea, and the southeast Indian Ocean. Thus, the model's AAIW formation process seems to be primarily following the circumpolar mechanism of Sverdrup et al. (1942), with some additional localized spiking from SAMW. This agrees with the study by Sørensen et al. (2001) in which midlatitude convection is reduced upon GM inclusion (see also Hirst and McDougall 1996; Duffy et al. 1999) thereby reducing the amount of diapycnal mixing in the region off the coast of Chile, in contrast to models without isopycnal and/or GM mixing (e.g., England 1992, 1993). In analyzing AAIW variability in the present paper we will focus our attention on ventilation along the $\sigma_{27.2}$ surface while acknowledging that lighter-density water, in particular SAMW, also contributes to ventilation in the model's intermediate layers. For studies of SAMW variability in observations and models the reader is referred to Rintoul and England (2002) and Bryden et al. (2003).

Since AAIW formation tends to occur in late winter when surface waters are at their most dense and mixed

layers are at their deepest, we use late-winter data for our analyses. For this purpose, we define "late winter" as the mean of September and October properties. The late-winter ocean variables (θ , S , u , and v) are mapped onto the $\sigma_{27.2}$ surface by means of spatial linear interpolation and averaging. A high-pass filter on the frequency domain is applied to the ocean data on the isopycnal to remove variabilities with period longer than 200 yr. A cosine taper is used to smooth the edge of the filter to reduce the effect of ringing or Gibb's phenomenon in the time domain (Emery and Thomson 1998). Complex empirical orthogonal function (CEOF) analysis in the time domain is used in this study to decompose the θ - S variability into orthogonal modes and to capture propagating signals as the domain of interest lies within the influence of the eastward-flowing Antarctic Circumpolar Current (ACC). The CEOF analysis has been used widely in climate studies (e.g., Mizoguchi et al. 1999; Putman et al. 2000); for a description of the CEOF technique the reader is referred to Barnett (1983) and Horel (1984). The power spectral density of each orthogonal mode's principal component time series is estimated using the Thomson multitaper

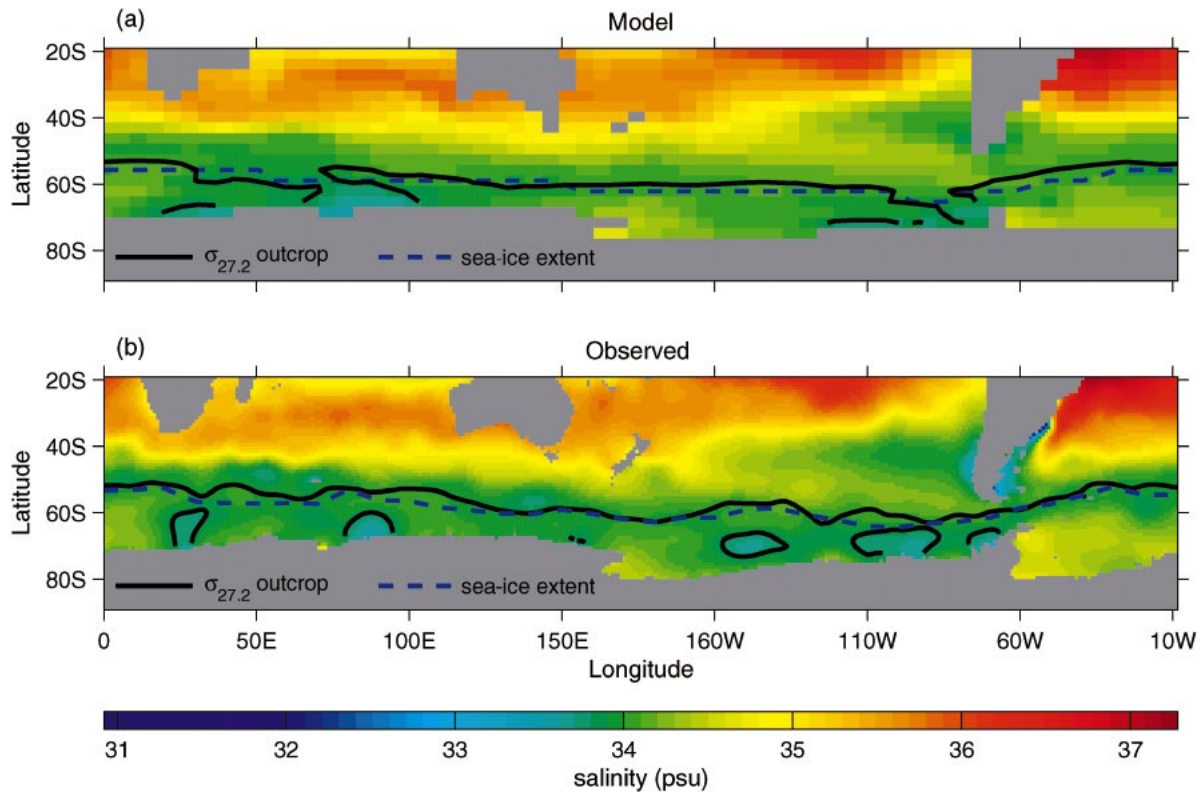


FIG. 2. Mean position of the late-winter $\sigma_{\theta} = 27.2 \text{ kg m}^{-3}$ outcrop (solid contour) and the maximum late-winter sea-ice extent (dashed contour) in (a) the model and (b) observations. The maximum late-winter sea-ice extent is the northernmost latitude of late-winter ice coverage (a) in the model over the full 1000-yr simulation and (b) observed during 1973–98. The color shading shows mean late-winter surface salinity values. The observed late-winter outcrop position is calculated using the Levitus climatology. For both model and observed, late-winter θ – S values are derived from a mean over Sep and Oct.

method described in Percival and Walden (1993, 330–374) and Mann and Lees (1996). Red-noise processes represent noise with low-frequency fluctuations resulting from the integration of white-noise forcing via slow ocean processes. The background spectrum of a first-order autoregressive (AR-1) red-noise process is estimated and fitted onto the total spectrum [using the robust method described in Mann and Lees (1996)] to provide

a basis for identifying significant AAIW variability beyond that of a red-noise signal at 95% confidence level.

c. Mechanisms forcing AAIW variability

The second part of our study is to explain the model θ – S variability in AAIW by examining water-mass variability at the $\sigma_{27.2}$ outcrop. This approach assumes that

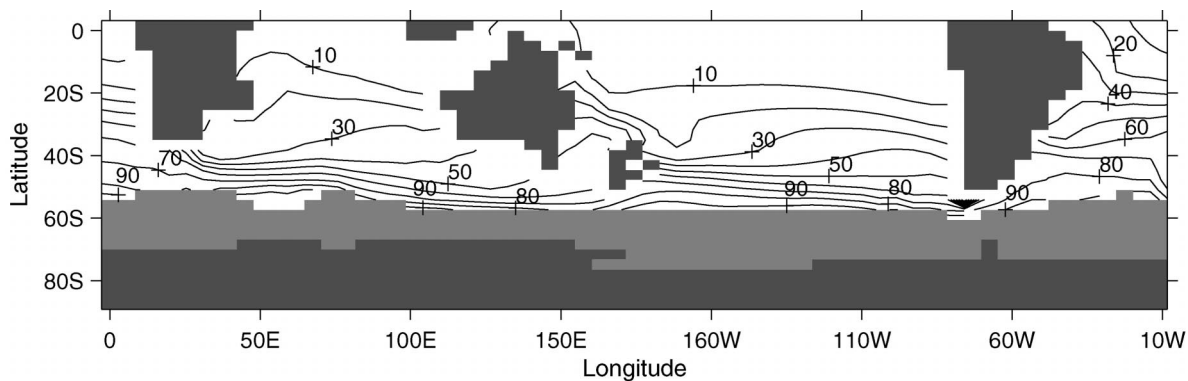


FIG. 3. Dye tracer concentration field (as a percentage) on $\sigma_{\theta} = 27.2 \text{ kg m}^{-3}$ ($\sigma_{27.2}$) after 50 yr of tracer release in the coupled climate model. Gray-shaded areas are poleward of the $\sigma_{27.2}$ outcrop.

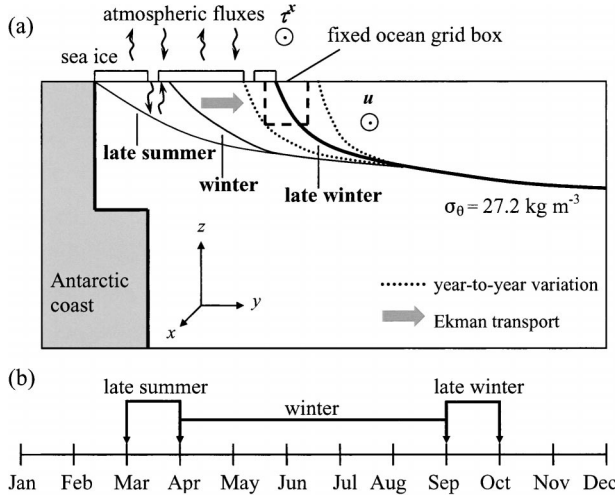


FIG. 4. (a) Schematic diagram illustrating processes in the high latitudes of the Southern Ocean that influence the location of the $\sigma_{\theta} = 27.2 \text{ kg m}^{-3}$ surface ($\sigma_{27.2}$). Note the seasonal and year-to-year displacement of the isopycnal. (b) Conventional season definitions used in the heat and salt budget analyses.

a substantial fraction of AAIW is sourced from AASW (via either direct subduction or cross-frontal mixing at the APFZ). This seems to be the case in the present model, because ventilation on the $\sigma_{27.2}$ surface is genuinely circumpolar, with only weak evidence of enhanced formation rates in mode water formation regions (see Fig. 3). We perform heat and salt budget analyses as in Rintoul and England (2002) using the following equations in which all of the surface variables have been interpolated onto the late-winter $\sigma_{27.2}$ outcrop:

$$\frac{\partial \theta}{\partial t} = \frac{Q_{\text{net}}}{\rho_0 C_p h} - \mathbf{u} \cdot \nabla \theta - w \frac{\partial \theta}{\partial z} + \theta'_{\text{mix}} \quad \text{and} \quad (1)$$

$$\frac{\partial S}{\partial t} = \frac{H_{\text{net}}}{h} - \mathbf{u} \cdot \nabla S - w \frac{\partial S}{\partial z} + S'_{\text{mix}}, \quad (2)$$

where θ and S are the surface layer temperature and salinity located at model grid 12.5-m depth, Q_{net} and H_{net} are the air–sea heat and salt fluxes, ρ_0 is density, which equals 1027.2 kg m^{-3} , C_p is the specific heat capacity of seawater (taken as $3986 \text{ J kg}^{-1} \text{ K}^{-1}$), h is surface layer thickness (25 m), $\mathbf{u} = (u, v)$ is horizontal velocity, w is vertical velocity, and θ'_{mix} and S'_{mix} are the heat and salt budget terms for mixing (vertical, isopycnal, convective, and GM).

The seasonal and year-to-year displacements of the $\sigma_{27.2}$ outcrop position are illustrated in Fig. 4a. The isopycnal outcrop moves with respect to sea surface conditions—in response to atmospheric forcings and ocean dynamics—in such a way as to conserve density by adjusting its geographical position. For example, following surface warming/freshening (cooling/salination) due to seasonal and year-to-year variations, the late-winter isopycnal outcrop would be displaced southward (northward). Hence to obtain heat/salt budget closure

on the late-winter $\sigma_{27.2}$ outcrop in each model year, the heat and salt content terms, $\partial \theta / \partial t$ and $\partial S / \partial t$, are calculated by subtracting late-summer θ – S (defined as the average over March and April) from late-winter θ – S on the annually fixed but zonally varying position of the late-winter $\sigma_{27.2}$ outcrop (∂t then ≈ 6 months). All variables on the right-hand side of Eqs. (1) and (2) are defined as the mean (winter) values averaged over April to September. The conventional season definition of the variables is shown in Fig. 4b. The budget equations then explain transformations in θ – S properties from late summer to late winter as a function of winter air–sea fluxes and ocean dynamical processes at the late-winter outcrop position for each year. It may be noted that the component of horizontal advection of heat and salt due to wind-driven Ekman transport can be calculated as $\mathbf{u}_e \cdot \nabla \theta$ and $\mathbf{u}_e \cdot \nabla S$, where $\mathbf{u}_e = (\tau^y / \rho f h, -\tau^x / \rho f h)$ with f being the Coriolis parameter.

The surface heat and salt flux terms can be further decomposed into their respective components:

$$Q_{\text{net}} = Q_{\text{solar}} - (Q_{\text{evp}} + Q_{\text{sh}} + Q_{\text{lw}}) - Q_{\text{oi}} \quad \text{and} \quad (3)$$

$$H_{\text{net}} = E - P + H_{\text{ice}}, \quad (4)$$

where Q_{solar} is the incoming solar radiation; Q_{evp} , Q_{sh} , and Q_{lw} are the sea-to-air heat flux terms: evaporative, sensible heat, and longwave radiation, respectively; Q_{oi} is the ocean-to-ice sensible heat flux; E and P are effective salt fluxes due to evaporation and precipitation; and H_{ice} is the salt flux due to sea-ice melting and formation. The role of sea ice is anticipated to be important in controlling the variability on $\sigma_{27.2}$ as the isopycnal breaks the surface near the Antarctic sea-ice margin in the model and in observations (as seen in Figs. 2a,b). Note that the outcrop can exist at more than one meridional location at certain longitudes (Figs. 2a,b) in which only the northernmost part contributes to AAIW. In such instances the heat/salt budget analyses are conducted only on the northernmost part of the $\sigma_{27.2}$ outcrop.

3. Model AAIW: Mean properties and circulation

a. Potential temperature and salinity

The structure of AAIW simulated by the model can be seen in Fig. 1 (left column), which shows the zonally averaged meridional section of late-winter salinity in each ocean basin. The corresponding observed salinity reproduced from the Levitus climatology is displayed in the right column of Fig. 1 for comparison. The $\sigma_{27.2}$ contour shown, indicating the isopycnal used for analysis in this study, marks the approximate core of AAIW, both in the model and observed, which extends down from the surface outcrop region at 60°S to intermediate depths of 700–1000 m. Overall AAIW representation is very good in the CSIRO climate model, though the northward extent of the simulated salinity minimum is weaker than the observed particularly in the Indian

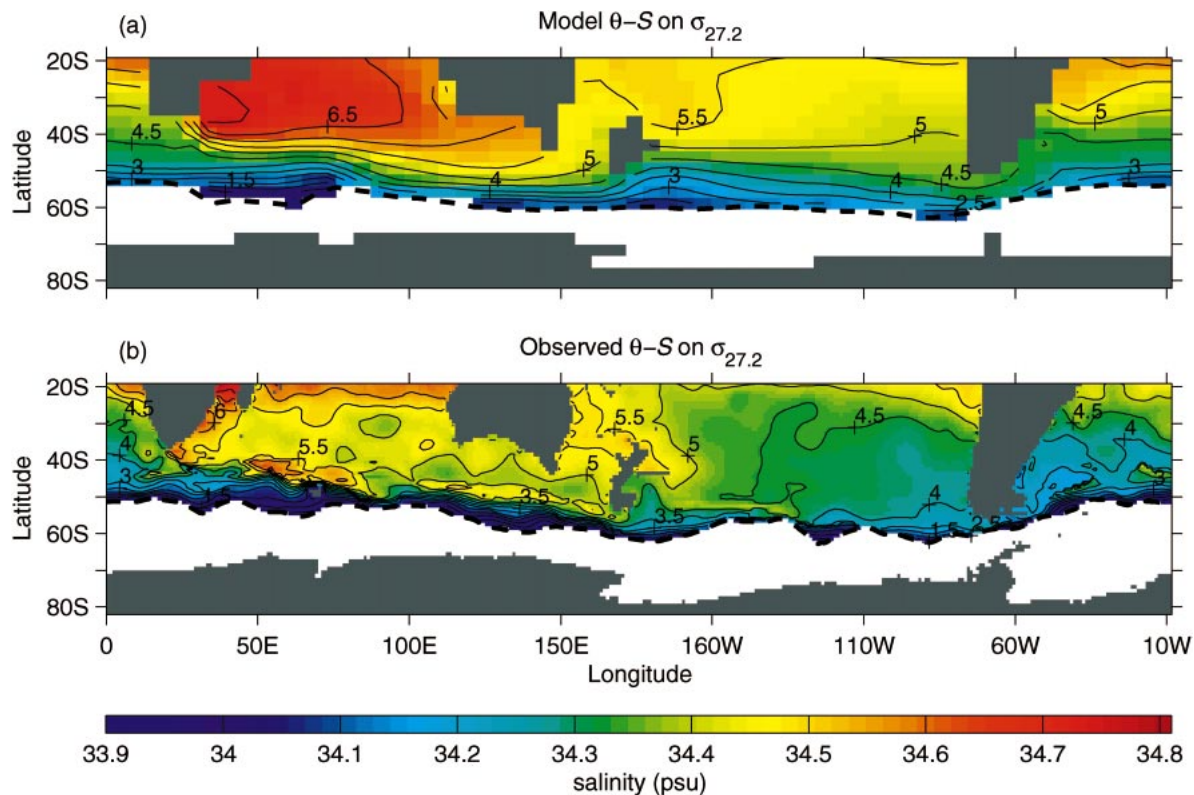


FIG. 5. Late-winter potential temperature (shown as contours) and salinity on $\sigma_{27.2}$ in (a) the model and (b) the observed Levitus climatology. The dashed contour marks the mean location of the $\sigma_{27.2}$ surface outcrop during late winter.

Ocean. The weak salinity minimum in the Indian Ocean appears to be due to unrealistically deep penetration of SAMW at 40° – 50° S, marked by a relatively deep mixed layer there in the model salinity field (Fig. 1, Indian Ocean panels). Weak northward penetration of AAIW has been a common problem in coarse-resolution ocean models, though improvement is realised here using zero horizontal diffusion and GM mixing. Overall the representation of AAIW shown in Fig. 1 is as good as can be expected in a climate model of coarse resolution.

The late-winter θ – S distribution along $\sigma_{27.2}$ in the model and observed is presented in Figs. 5a and 5b, respectively. Values of θ – S discussed here are those found on the $\sigma_{27.2}$ surface, unless otherwise specified. In both model and observations, relatively cold and fresh water of 1.0° – 2.0° C and 33.90–34.10 psu is found near the outcrop region. Temperature and salinity increase northward with depth as AASW mixes with adjacent waters during its subduction into the interior. The coldest and freshest AAIW variety on $\sigma_{27.2}$ is found in the Atlantic sector with salinity fresher than 34.4 psu as far north as 43° S. The model Atlantic basinwide-averaged θ – S at 43° S is 4.5° C and 34.32 psu at ≈ 600 -m depth, in reasonable agreement with the corresponding observed values of 3.9° C and 34.26 psu. The Indian sector AAIW is the warmest and saltiest variety; for

example the basinwide-averaged θ – S values at 43° S are 5.6° C and 34.51 psu at 800-m depth. Farther to the north at 30° S, the Indian Ocean AAIW has typical $\theta > 6.0^{\circ}$ C and $S > 34.60$ psu, which is warmer and saltier than observed because of excessive overturn of SAMW (see Fig. 1). The depth of the $\sigma_{27.2}$ surface in this region is also generally about 100 m shallower than observed (Fig. 1), overlying the model's S minimum. In contrast, the core of AAIW in the Pacific coincides well with the $\sigma_{27.2}$ surface. There, model θ – S values are in fairly good agreement with the observed, albeit a little warmer and saltier because of a weaker northward penetration of AAIW in the model. The Atlantic AAIW is slightly cooler and fresher than its counterpart in the Pacific. Abrupt changes in θ – S properties at transition regions between ocean basins are seen in both the model and observations. Despite the generally warmer and saltier nature of model AAIW on $\sigma_{27.2}$, its qualitative spatial variation is consistent with the observations of Georgi (1979), Piola and Georgi (1982), and the Levitus climatology.

b. Circulation

The simulated mean circulation along $\sigma_{27.2}$ to the north of the polar front (PF) is shown in Fig. 6. Note

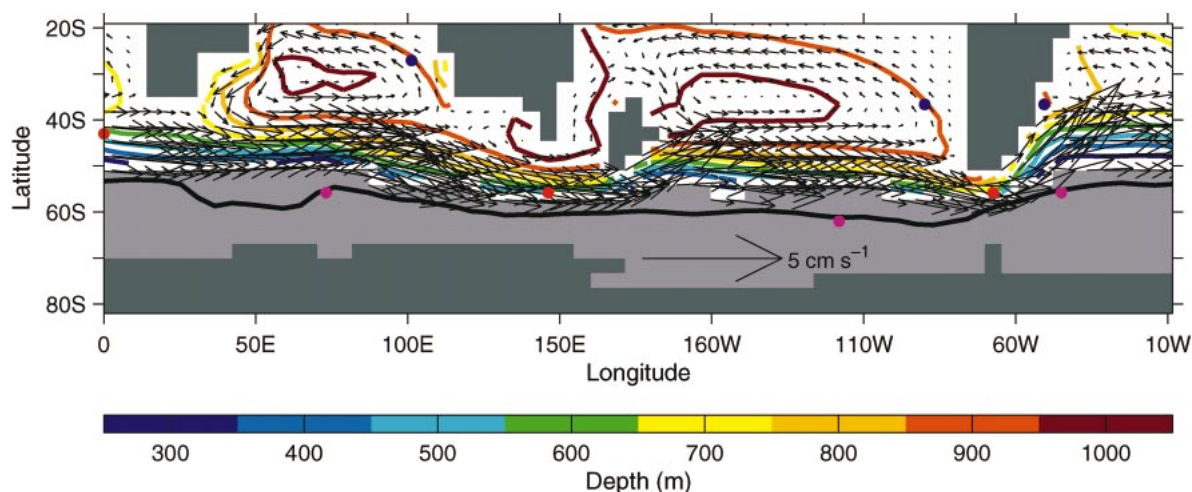


FIG. 6. Mean circulation on the $\sigma_{27.2}$ density surface shown by late-winter velocity vectors averaged over 1000 yr. Velocity fields are shown only at depths below 200 m. Depth contours are shown in colors. Mean position of the late-winter $\sigma_{27.2}$ outcrop is shown by the black contour. Colored dots indicate locations of θ - S scatterplots in Fig. 7, shown later.

that along the isopycnal layer, depth increases northward from approximately 200 m along the northern flank of the PF to 1000 m to the north of 40°S. The magnitude of current velocities decreases with the northward increase of depth. The strongest current with zonal velocity of approximately 5 cm s^{-1} occurs within the influence of the ACC south of 40°S, transporting the water mass along $\sigma_{27.2}$ eastward in a circumpolar manner. In the south Pacific, two branches of intermediate water transport exist in the southeastern region. The northern branch channels the intermediate water northward by the eastern boundary current as part of the subtropical South Pacific gyre (as in England et al. 1993). The southern branch transports the intermediate water eastward by the ACC through the Drake Passage turning northward as it flows into the South Atlantic. There, part of the intermediate water is deflected to the north joining the subtropical South Atlantic gyre. Northern and southern branches are visible at about 25°S, 40°W along the western boundary current, as documented by the observations of Schmid et al. (2000). Gordon et al. (1992) found a significant interocean exchange of thermocline and intermediate water between the South Indian and South Atlantic Oceans within the Benguela Current. However, our model does not resolve this westward transport of saline water from the evaporative Indian Ocean. The model does capture a southwestward flow as part of the subtropical gyre at about 35°S just to the southeast of Africa (Fig. 6), though no Indian to Atlantic leakage occurs via westward advection. A final feature of AAIW circulation worth noting in Fig. 6 is the northward flow in the Tasman Sea along $\sigma_{27.2}$. This pathway is similar to that proposed by Sokolov and Rintoul (2000) and Rintoul and Sokolov (2001), though in the model transport persists much farther to the north.

4. Model AAIW: Interannual to centennial variability

a. θ - S properties

We now turn our attention to the magnitude and structure of θ - S variability simulated in the coupled climate model. Temperature-salinity scatterplots presented in Fig. 7 show the spread of θ - S properties over 1000 yr both on $\sigma_{27.2}$ (marked with crosses) and at constant depths (marked with dots) at chosen locations in the Southern Ocean (see Fig. 6 for geographic positions). Locations are selected to give representation of (i) AASW in each ocean sector (left column of Fig. 7), (ii) AAIW at about 500-m depth downstream of these AASW locations (middle column of Fig. 7), and (iii) AAIW variability at about 900-m depth in regions of relatively rapid renewal (right column of Fig. 7). Variability at fixed grid points (i.e., at constant z levels) is presented for comparison with variability along isopycnals to provide a more complete picture of the scale of variability in both z and $\sigma_{27.2}$ space (see also, e.g., Bindoff and McDougall 2000; Arbic and Owens 2001). The θ - S variability on fixed z levels is obtained by tracking changes along the salinity minimum level closest to $\sigma_{27.2}$ without interpolation between model grid points. Therefore, by implication of the model's coarse resolution, some of the θ - S scatterplots shown have slightly higher or lower mean density than 27.2 kg m^{-3} .

The θ - S diagrams in Fig. 7 demonstrate how the properties of the simulated water mass along $\sigma_{27.2}$ vary in space and time. The range of AASW θ - S variability on the $\sigma_{27.2}$ outcrop at the locations shown (left column of Fig. 7) is up to 5°C and 0.5 psu. The Pacific sector exhibits the largest AASW θ - S variability, this range then progressively decreases eastward into the Atlantic

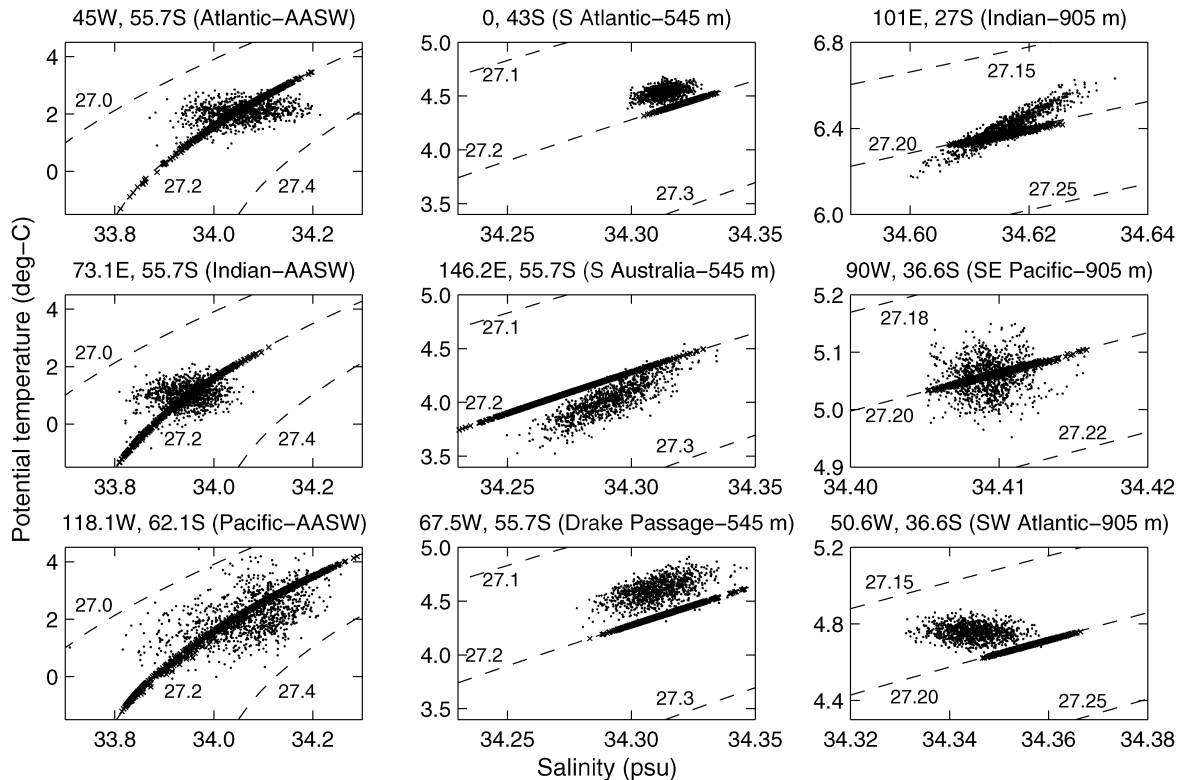


FIG. 7. 1000-yr θ - S scatterplots at specified ocean grid boxes (shown in Fig. 6) having density closest to $\sigma_\theta = 27.2 \text{ kg m}^{-3}$ (marked with dots) and along the isopycnal (marked with crosses), at the surface (left), 545 m (middle), and at 905 m (right). Note that at the surface the scatterplot along the $\sigma_{27.2}$ isopycnal varies with latitude, and in the interior it varies with depth.

and Indian Oceans. The AASW variability at fixed locations is smaller than along the $\sigma_{27.2}$ isopycnal, which suggests variations in the latter are mainly due to interannual meridional displacement of the outcrop position. This is supported by a strong positive correlation (≈ 0.9 correlation coefficient) between along-isopycnal θ - S variations and meridional displacement of the late-winter outcrop around Antarctica. The positive correlation implies that the outcrop generally moves southward (northward) with decreasing (increasing) surface θ - S along the isopycnal, in response to variations in surface forcing and/or Ekman transport.

While the surface outcrop displaces meridionally, the isopycnal surface at depth can move upward and downward in response to interior dynamics (Fig. 4). At 545-m depth, θ - S variability is much smaller than the variability at the surface, with an along-isopycnal range of $0.2^\circ\text{--}0.7^\circ\text{C}$ and $0.03\text{--}0.10$ psu (comparable to the magnitude of variability along isobars). The variability is largest south of Australia and decreases into the Drake Passage and the South Atlantic. The comparable magnitude of variability along the $\sigma_{27.2}$ isopycnal with that on fixed z levels suggests that the variability of AAIW at this depth can be explained largely by changes along the isopycnal, which is most likely to be driven by changes in surface properties at the isopycnal outcrop (Bindoff and McDougall 1994). Down to 900-m depth,

θ - S variability decreases further, with an along-isopycnal range of order 0.1°C and $0.01\text{--}0.02$ psu. This is now smaller than the fixed z -level range of order $0.2^\circ\text{--}0.5^\circ\text{C}$ and $0.01\text{--}0.03$ psu. The larger variability on isobars is most easily explained by variability in the circulation of the subtropical gyres, which forces “heaving” of the isopycnal surfaces (see Bindoff and McDougall 1994), superimposed on the changes along the isopycnal itself.

b. Comparison with observations

It is worth commenting that the size of decadal changes along $\sigma_{27.2}$ in the model is generally weaker than the observations documented earlier in section 1. Changes over 22–25 yr in the model at the observed regions show maximum basin-scale cooling and freshening of the order 0.05°C and 0.010 psu. More specifically, the strongest 20-yr freshening and cooling over the model’s 1000-yr record along $\sigma_{27.2}$ in the Indian Ocean (32°S ; 0.05°C , 0.007 psu), southwest Pacific (0.07°C , 0.009 psu along 170°W), and the southwest Atlantic (32°S ; 0.07°C , 0.011 psu) are weaker than observed (e.g., Bindoff and McDougall 2000; Johnson and Orsi 1997; for values, see section 1). In the Tasman Sea, the maximum model cooling and freshening (0.08°C , 0.014 psu) are comparable to changes documented by Bindoff and Church (1992). The weaker changes in our model as compared

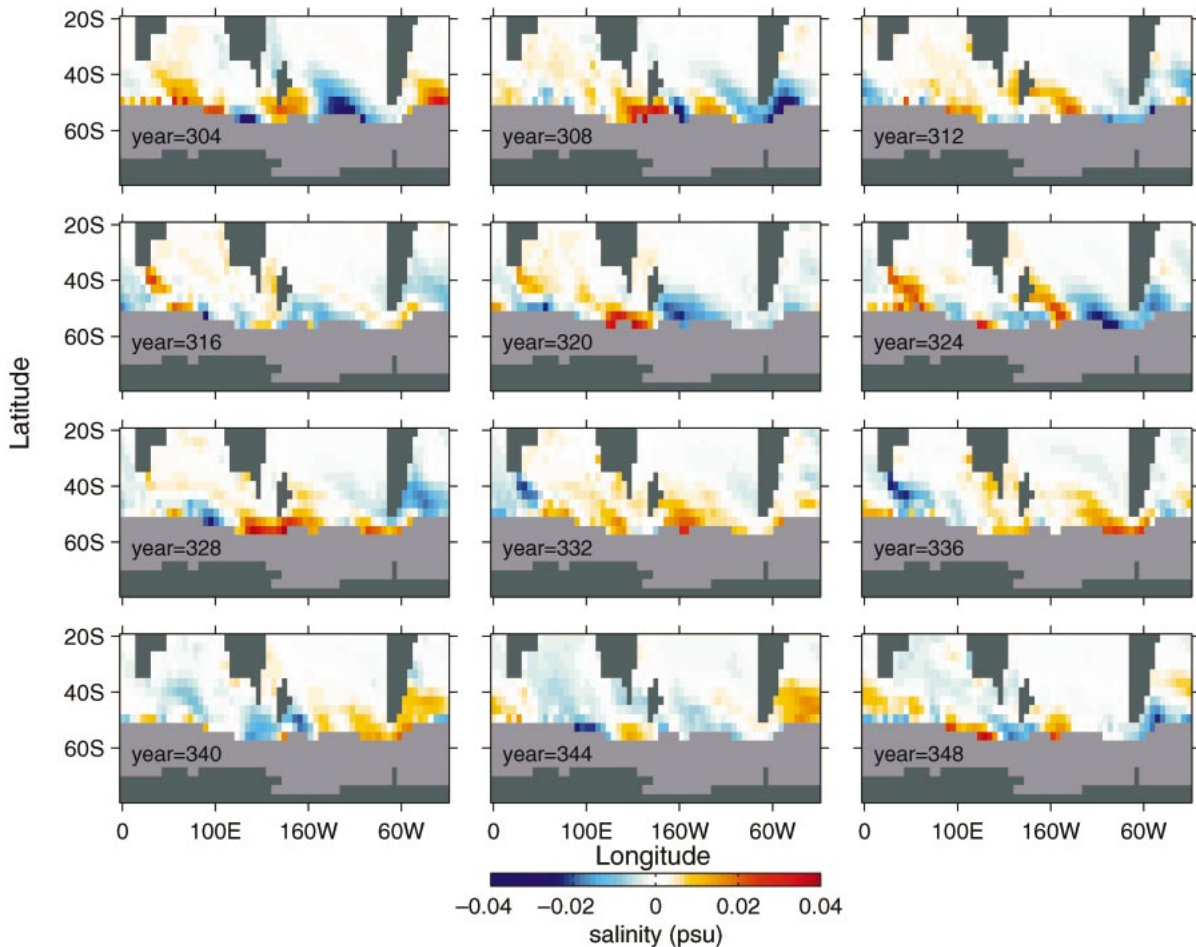


FIG. 8. Late-winter salinity anomaly along $\sigma_{27.2}$ from year 304 to year 348 in a 4-yr interval. Gray-shaded areas denote regions south of the CEOF domain (base of the $\sigma_{27.2}$ mixed layer).

with the observed support the argument that an anthropogenic climate change signal is detectable in the observations, as also suggested by Banks et al. (2000). However, we note that the weaker model variability may also be due to the climate model heat and freshwater flux adjustment terms, which tend to damp θ - S variability at the sea surface.

c. Propagation of θ - S anomalies

The variability of θ - S properties shown in Fig. 7 propagates eastward with the ACC as well as northward at certain longitudes (refer also to Fig. 6). In this section we analyze how θ - S anomalies propagate along the $\sigma_{27.2}$ isopycnal surface in the model. We define the local θ - S anomalies as the deviation of the late-winter θ - S values from their long-term 1000-yr (late winter) means. Figure 8 shows a typical 60-yr record of $\sigma_{27.2}$ AAIW salinity anomalies in 4-yr increments (by density conservation we need not show θ). It can be seen from the time series that this region is characterized by eastward-propagating signals of anomaly with magnitude of the

order of 0.02–0.04 psu (matching θ anomalies of 0.2°–0.4°C, figure not shown). The eastward-propagating signals can bifurcate into northward flow—for example, if blocked by eastern continental boundaries. One such case is seen in the South Pacific during years 304–308 when a strong negative anomaly (freshening and cooling) centered at approximately 120°W splits to flow northward along the coast of Chile as well as continuing through the Drake Passage into the Atlantic (year 312). Note that the magnitude of anomalies decreases with northward flow because of the mixing of water masses. Another example of an apparent propagation of anomaly can be seen during years 320–336 originating south of New Zealand. In year 320, a significant warm, salty anomaly sits southwest of New Zealand, just upstream from a notable cold, fresh signal. During the next 16 yr this dipole signature can be seen propagating eastward and then northward in the South Pacific subtropical gyre. Note that northward-propagating anomalies can also be seen in the Tasman Sea along the east coast of Australia, as well as in the Indian (years 336–348) and Atlantic sectors (years 324–332).

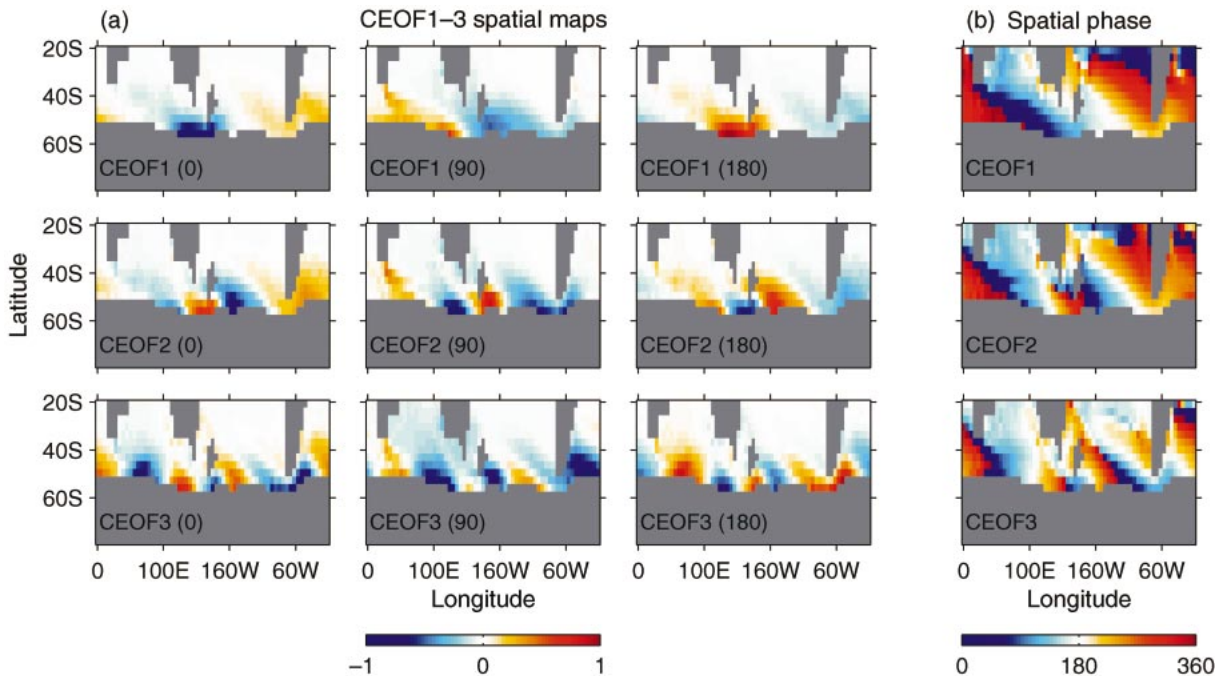


FIG. 9. (a) The first three complex EOF modes of salinity shown at 90° phase intervals along $\sigma_{27.2}$. The three modes account for a total of 53% of the net S variance on $\sigma_{27.2}$. The first (CEO1), second (CEO2), and third (CEO3) modes account for 24%, 16%, and 13%, respectively. An equivalent CEOF analysis of θ on $\sigma_{27.2}$ shows similar modal structure and so is not shown here. (b) Spatial phase angle of CEO1-3 indicating the direction of phase propagation of each mode from 0° to 360° . Apparent phase discontinuities occur because the phase is defined only between 0° and 360° .

d. Complex EOF analysis

To summarize the structure of θ - S anomaly propagation along the $\sigma_{27.2}$ isopycnal, and how this evolves in space and time, we now employ complex empirical orthogonal function analyses. To avoid biasing the CEOFs to the surface layer variability where meridional displacement of the isopycnal occurs, we analyze the $\sigma_{27.2}$ isopycnal from below the base of the winter mixed layer. The shallowest depth in the CEOF analysis is at about 200 m. The pattern of each successive CEOF mode of temperature turns out to be virtually identical to that of salinity, with the corresponding principal component time series highly positively correlated at zero lag. Thus, we refer only to the CEOF modes of salinity in our discussion. This similarity of pattern in the θ and S modes is because a change in temperature along the AAIW isopycnal must be accompanied by a corresponding change in salinity, so that density remains unaltered by variability in θ - S .

Because most of the AAIW θ - S variance is contained to the south, it is expected that the decomposition of the first few CEOF modes will mainly resolve the eastward propagation of anomalies within this region. Figure 9a presents the first three dominant orthogonal modes of salinity anomaly, explaining 53% of the total salinity variance on $\sigma_{27.2}$. Each mode is presented at a phase interval of 90° , showing a clear eastward propagation of anomalies. This eastward propagation is also

implied by the spatial phase maps showing increasing phase eastward within the circumpolar region and northward into the ocean interior (Fig. 9b). The eastward propagation of anomalies is due to the dominant influence of the ACC. Other studies also document eastward-propagating anomalies of ocean surface variables in observations (e.g., White and Peterson 1996) and in model simulations (e.g., Bonekamp et al. 1999; Cai et al. 1999). The magnitude of the CEOF modes decreases northward with increasing depth, in part due to background mixing in the model, which tends to damp interior θ - S variability.

The first CEOF mode shows an eastward-propagating wavenumber-1 pattern (Fig. 9a), accounting for 24% of the total variance. Temporal characteristics of the first mode are presented in Fig. 10 (left column) showing the real part of the first principal component (PC1) time series, its power spectral density, and the temporal phase function. The dashed curve superimposed on the power spectrum indicates the 95% confidence limit of the estimated background noise. This first CEOF mode is dominated by signals with decadal to interdecadal periods. The variance is weighted increasingly toward the low-frequency fluctuations up to an equivalent of a 62.5-yr period. The estimated 95% confidence level of the background noise suggests that the periods longer than 20 yr are not different from red noise, which can be interpreted as an integrated white-noise forcing trans-

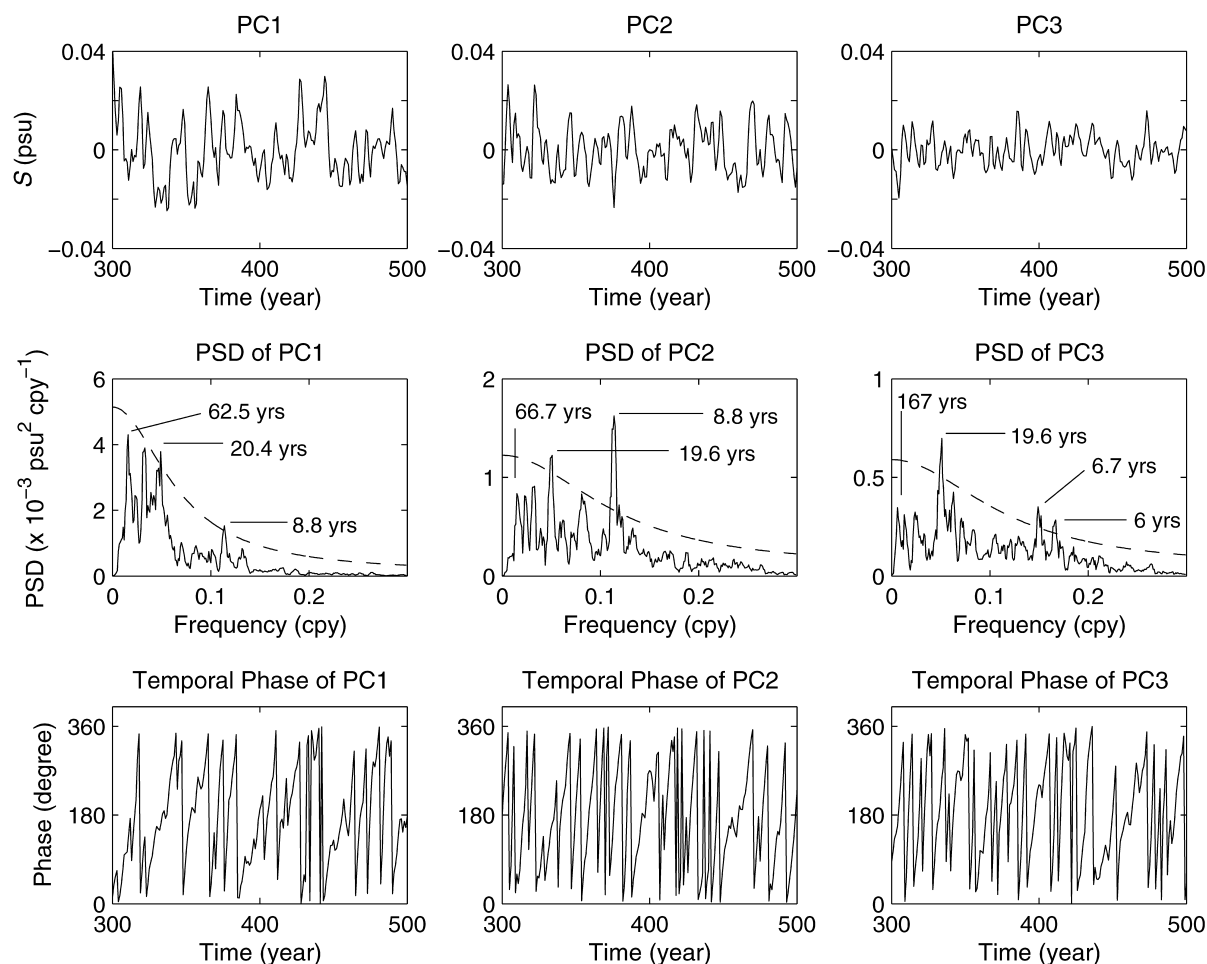


FIG. 10. (top) Principal component time series of CEOF1–3 displayed from year 300 to 500. (middle) Power spectral density (PSD) of the principal component time series with an estimated AR-1 background spectrum at 95% confidence level (dashed curve). (bottom) Temporal phases obtained from CEOF1–3 displayed from year 300 to 500. The temporal phase angles in the lower panels are defined between 0° and 360° .

mitted from the outcrop region via ocean mixing and processes. The ≈ 9 - and 20-yr cycles, however, are significantly above the background noise and are most likely to be related to θ – S variability transmitted from the surface. A correlation analysis between the real and imaginary part of PC1 suggests an approximate 2–3-yr interval for each 90° phase. This suggests it takes about 8–12 yr for the wavenumber-1 signal to encircle the globe, matching the approximate advective time scale of the ACC at the surface. However, this phase speed estimation is not accurate because it is biased toward the higher-frequency components of the time series. The temporal phase of PC1 shown in Fig. 10 (lower-left panel) suggests a large variation in the period of the first mode ranging from decadal to interdecadal time-scales, with irregularity in phase speed. This estimation using the temporal phase function takes into account the slowly propagating components and results in a slower average phase speed—on the order of 0.03 m s^{-1} (matching current velocities at depth $\approx 400 \text{ m}$ along $\sigma_{27.2}$).

The second CEOF mode shows a propagating wavenumber-2 pattern. This mode accounts for 16% of the total salinity variance on $\sigma_{27.2}$. The power spectral density for the second mode (Fig. 10, middle column) shows a dominant peak at 9-yr period, which for a wavenumber-2 pattern means the anomaly will take approximately 18 yr to encircle the globe. This phase speed matches the propagation rate of the ACC at the base of the winter mixed layer ($\approx 200 \text{ m}$). As we have presented previously, the typical zonal current velocity at about 200-m depth along the isopycnal is about 5 cm s^{-1} , which implies about 16 yr to complete one circumpolar cycle at 50°S . However, there is also a significant signal at 20-yr period above the 95% confidence limit of estimated background noise (Fig. 10, middle panel). Variability at longer periods is also noted, though not significantly distinct from red-noise processes. The wavenumber-2 pattern suggests this mode is related to Antarctic Circumpolar Wave (ACW)-like signals transmitted along the intermediate water isopycnal layer. Bo-

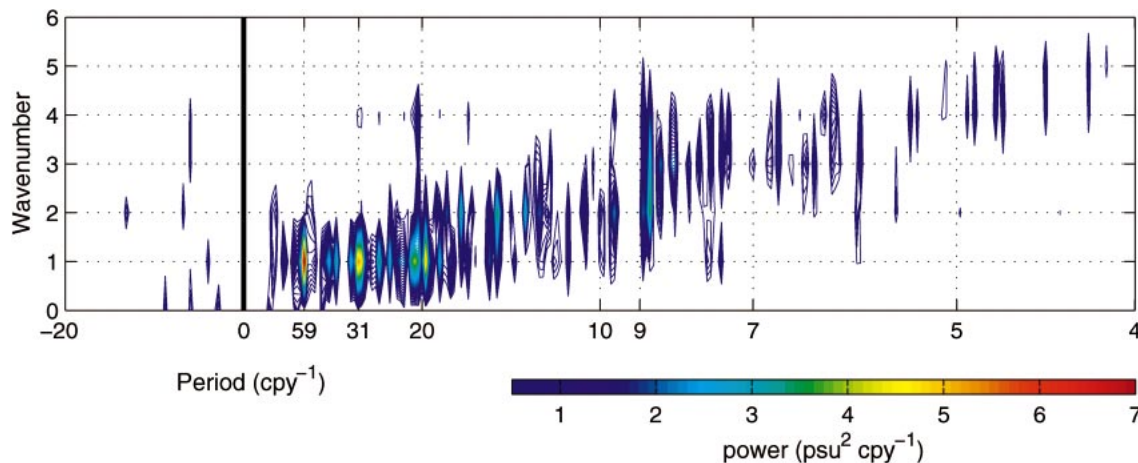


FIG. 11. Frequency–wavenumber spectrum of salinity anomaly along the southernmost boundary of the CEOF domain on $\sigma_{27.2}$. The analysis decomposes spatial–temporal signals and shows mostly eastward-propagating components (positive frequencies).

nekamp et al. (1999) show from their hindcast run that ACW-like signals are detectable in the deeper ocean with similar frequency and patterns as the surface signals, but with phase shifts and a reduced amplitude. The standing period of the interior signal is about 2 times that of the surface ACW signal found by White and Peterson (1996), which propagates eastward at average speeds of $6\text{--}8\text{ cm s}^{-1}$ to take $8\text{--}10\text{ yr}$ for each phase to travel around the globe.

The third CEOF mode on $\sigma_{27.2}$ shows a propagating wavenumber-3 pattern and explains 13% of the total variance. Variability related to the third mode is distributed over interannual to centennial time scales (Fig. 10, right column). There are significant spectral peaks at about 20-yr period and at $\approx 6\text{--}7\text{-yr}$ periods (i.e., the peaks appearing above the 95% confidence limit of background noise). The longer time-scale periodicity of order $50\text{--}150\text{ yr}$ is not significantly distinct from a red-noise process and is likely to be associated with northward mixing along isopycnals (particularly in the Indian basin, Fig. 9). For example, it takes about 80 yr for a $\theta\text{--}S$ anomaly to be mixed a distance of 20° latitude using a scale mixing distance of $\Delta y \approx (2\kappa t)^{1/2}$, where $\kappa = 1 \times 10^7\text{ cm}^2\text{ s}^{-1}$ is the model isopycnal diffusivity and t is time. The shorter-period energy of the wavenumber-3 CEOF (PC3) is likely associated with the model equivalent of the ACW. For example, Cai et al. (1999) found a predominant quasi-stationary wavenumber-3 pattern with standing oscillation of $4\text{--}5\text{ yr}$ using 60 yr of SST and SSS data in the earlier version of CSIRO climate model. They filtered all variability outside the time scale of $1\text{--}10\text{ yr}$. This wavenumber-3 pattern would thus take $12\text{--}16\text{ yr}$ to encircle the Antarctic continent. Cai et al. (1999) relate this mode to the ACW marked by the advection of SST anomalies by the surface ACC. The dominant shorter periodicity of the third mode that we find here ($6\text{--}7\text{ yr}$) is slightly longer than that of the Cai et al. (1999) ACW. This difference is likely due to the

different mixing schemes used in the two models; in particular our model employs GM whereas Cai et al. (1999) do not, and GM tends to decelerate the ACC.

The results of the CEOF analyses can be summarized in a frequency–wavenumber spectrum of signals along the southernmost boundary of the CEOF domain (shown in Fig. 11). The spectrum decomposes the variance in terms of wavenumber and frequency and partitions the total variance into contributions from eastward- and westward-traveling signals (refer to Storch and Zwiers 1999). As we can see from Fig. 11, the energy of the spectrum is dominated by eastward-traveling waves and is notably high between 20 and 60 cpy^{-1} with a wavenumber-1 spatial pattern. Decreasing variance is explained with increasing frequency implying the dominance of low-frequency processes along this region. Wavenumber-5 patterns are the highest wavenumber to appear in the analysis, though these explain only a very small amount of the total variance. Eastward-propagating wavenumber-4 and -5 appear in the 5th and 7th CEOF modes (not shown), accounting for 6% and 3% of the total variance respectively. It is worth mentioning that the fourth and sixth CEOF modes (also not shown) are nonpropagating modes. The fourth mode, accounting for 9% of total variance shows a standing-wave fluctuation with a more-or-less uniform circumpolar (wavenumber 0) pattern. This mode is not significantly different (at 95% confidence level) from a red-noise AR-1 process, suggesting integrated white noise via oceanic mixing. CEOF6 (4% of total variance) shows a standing-wave fluctuation at multidecadal–centennial time scales, concentrated at the tip of South Africa (see Fig. 8, years 316–336). This region is characterized by relatively large standard deviations of $\theta\text{--}S$ (figure not shown), a result of the sharp front between the warm salty Agulhas Current and the cold, fresh South Atlantic Current; $\theta\text{--}S$ variability in this region is influenced by fluctuations in the strength of these currents.

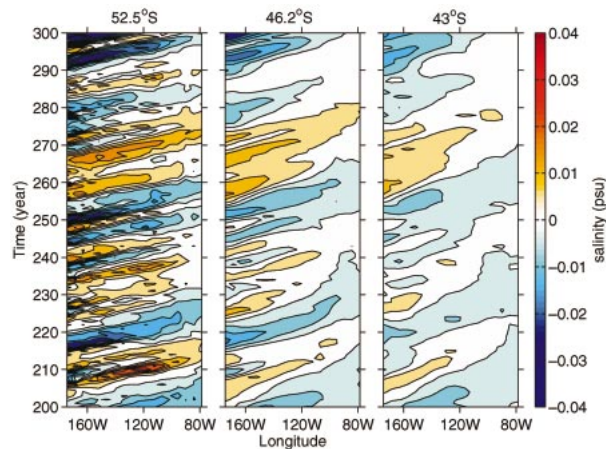


FIG. 12. Hovmöller diagram of salinity anomaly on $\sigma_{27.2}$ in the South Pacific between 180° and 80° W at 52.5° , 46.2° , and 43° S. Note that the depth of the isopycnal increases northward with average depths of 554, 884, and 963 m for each of the latitudes.

To further assess the propagation characteristics of interior anomalies, a Hovmöller diagram is shown in Fig. 12 of the salinity anomaly on $\sigma_{27.2}$ in the Pacific across approximately 180° – 80° W at three different latitudes. This figure shows that the period and spatial pattern of the anomaly vary with increasing depth. Thus, the speed of the propagating anomaly is affected by the decreasing speed of the ACC with depth, in contrast to the studies by Bonekamp et al. (1999) and Cai et al. (1999). This mismatch results because our analyses are based on interannual to centennial time scales, while only periods less than 10 yr are taken into account by Bonekamp et al. (1999) and Cai et al. (1999). Ocean mixing, a more gradual process than advection, results in a shift in spectral energy toward low frequencies (red spectrum). In our case, variability is gradually dominated by low frequencies of multidecadal to centennial time scales with increasing depth as advection effects decrease, allowing mixing to play a greater role. Indeed, the spectral energy of interannual and interdecadal time-scale processes (due to surface forcing and subsurface advection) become relatively small at the deeper reaches of AAIW (figure not shown). Since phase speed is a function of frequency, the phase speed of the anomaly is thus seen to increase with depth as shown in Fig. 12. Note also the phase shifts and reduction in the anomaly amplitudes with depth. In addition, the northwestward lag shown in the spatial CEOF patterns in Fig. 9a is also due to the time taken for the anomaly to be transmitted from the surface into the interior.

5. Mechanisms of variability

Under a *circumpolar* view of AAIW formation (e.g., Sverdrup et al. 1942; Sørensen et al. 2001), the surface forcing and/or ocean dynamics at the AAIW outcrop region play a crucial role in controlling intermediate

TABLE 1. Standard deviation of surface heat budget terms over 1000 yr zonally averaged over the late-winter $\sigma_{27.2}$ outcrop position. The $\partial\theta/\partial t$ term is obtained by subtracting late-summer temperature from late-winter temperature. All other terms are the average over Apr–Sep. The zonal Ekman advection term is significantly smaller than the total zonal advection term and hence is not presented. The standard deviation of heat flux components is provided. Values for the $\sigma_{26.9}$ outcrop are displayed for comparison.

Budget term	$\sigma_{27.2}$ ($\times 10^{-7}$ $^\circ\text{C s}^{-1}$)	$\sigma_{26.9}$ ($\times 10^{-7}$ $^\circ\text{C s}^{-1}$)
$\partial\theta/\partial t$	0.28	0.20
Zonal advection ($u\partial\theta/\partial x$)	0.15	0.16
Meridional advection ($v\partial\theta/\partial y$)	0.45	0.58
Meridional Ekman advection ($v_e\partial\theta/\partial y$)	0.44	0.57
Vertical advection ($w\partial\theta/\partial z$)	4.6×10^{-3}	4.8×10^{-3}
Net surface heat flux (Q_{net})	1.18	0.89
Air-to-ocean solar radiation (Q_{solar})	0.66	0.33
Ocean-to-air longwave radiation (Q_{lw})	0.40	0.25
Ocean-to-air sensible heat flux (Q_{sh})	0.87	0.42
Ocean-to-air evaporative heat flux (Q_{evp})	0.48	0.59
Ocean-to-ice sensible heat flux (Q_{oi})	0.13	1.2×10^{-5}

water variability at depth. Even under a *noncircumpolar* formation view (e.g., McCartney 1977; England et al. 1993), with mode waters subducted and/or convected at preferential locations, variability in the surface outcrop region still controls variability in the interior via cross-front processes at the APFZ. To investigate mechanisms of AAIW variability, we therefore perform heat and salt budget analyses in terms of θ – S changes on the late-winter $\sigma_{27.2}$ outcrop, as described in section 2. This analysis is thus focused on the variability of Antarctic Surface Water, rather than other AAIW ingredients, such as SAMW [which is studied by Rintoul and England (2002)]. Note that significant year-to-year variations in the location of the late-winter outcrop occur, with mild (severe) winters resulting in poleward (equatorward) excursions of the $\sigma_{27.2}$ outcrop. Also, at particular locations where the Antarctic coast extends farther to the north (e.g., the Antarctic Peninsula and off East Antarctica between 50° and 100° E), the $\sigma_{27.2}$ layer does not necessarily outcrop throughout the full 1000 yr of model simulation. This will occur during years of mild winter conditions. In such instances no heat budget calculations are made during the years of no winter outcrop.

To summarize the magnitude of variability of each process, the zonally averaged standard deviation of the heat budget terms is given in Table 1. An attempt is made to calculate all the terms in Eq. (1), except for θ'_{mix} , because mixing in the model tends to damp anomalies rather than create them (see also Rintoul and England 2002). The net surface heat flux term has the highest standard deviation in comparison to the other budget terms. This suggests that the anomalies created by surface heat fluxes dominate the variability of AAIW sourced at the $\sigma_{27.2}$ outcrop. The heat storage rate term ($\partial\theta/\partial t$) is much smaller than the net heat flux term (Q_{net}), confirming that mixing plays an important role in damping anomalies in the model. Northward Ekman transport

TABLE 2. Standard deviation of surface salinity budget terms at the $\sigma_{27.2}$ and $\sigma_{26.9}$ outcrops. The terms are calculated as for those in Table 1. The zonal Ekman advection term is significantly smaller than the total zonal advection term and hence is not presented. For consistency of units, evaporation and precipitation have been converted to equivalent salt fluxes (psu s^{-1}).

Budget term	$\sigma_{27.2}$ ($\times 10^{-8}$ psu s^{-1})	$\sigma_{26.9}$ ($\times 10^{-8}$ psu s^{-1})
$\partial S/\partial t$	0.35	0.32
Zonal advection ($u\partial S/\partial x$)	0.29	0.38
Meridional advection ($v\partial S/\partial y$)	0.39	0.67
Meridional Ekman advection ($v_e\partial S/\partial y$)	0.36	0.66
Vertical advection ($w\partial S/\partial z$)	4.9×10^{-3}	3.8×10^{-3}
Net surface salt flux (H_{net})	0.85	0.77
Evaporative salt flux (E)	0.27	0.33
Precipitative salt flux (P)	0.24	0.27
Ice-to-ocean salt flux (H_{ice})	1.66	4.0×10^{-3}

also contributes significantly to the variability. Vertical Ekman advection (Ekman pumping), on the other hand, makes little contribution to the variability at this layer. Zonal advection has a relatively small magnitude of variability on the zonal mean but, as we shall see below, plays an important role in some locations. This suggests that the ACC contributes, to some extent, to the variability at the outcrop layer. Table 1 also provides the breakdown of surface heat flux components of Eq. (3). Variability of the ocean-to-ice sensible flux Q_{oi} is small in comparison with the variability of the air–sea heat fluxes, and so wintertime θ variability is likely controlled by atmospheric (not ice) heat fluxes at the $\sigma_{27.2}$ outcrop. The air–sea heat flux components have comparable magnitudes of variability at the $\sigma_{27.2}$ outcrop, with the sensible heat flux (Q_{sh}) and the solar heat flux (Q_{solar}) the larger of the four terms.

A similar table for salinity flux terms is shown for the $\sigma_{27.2}$ outcrop region in Table 2. The net surface freshwater flux has the largest variability in comparison to the other salt budget terms. This suggests that surface freshwater fluxes have a major influence on the variability of AASW in the model. Among the surface freshwater flux terms, variability in the ice–ocean flux contributes most to the variability of AASW, as suggested by the highest standard deviation of that term (Table 2). This suggests that sea ice plays a major role in salinity variability at the outcrop region of the $\sigma_{27.2}$ isopycnal surface. This is not surprising given the close proximity of the outcrop location to the maximum sea-ice extent in both the model and observations (Fig. 2). The result is also consistent with the coupled model analyses of Saenko and Weaver (2001), who found mean AAIW S properties to be set, in part, by sea-ice processes. The meridional Ekman advection term is also significantly high in the model, implying that it too plays an important role in controlling the variability of S at the outcrop region. The zonal advection also plays an important role, with the fraction of salt storage rate variability higher than that in the heat budget. This is probably because

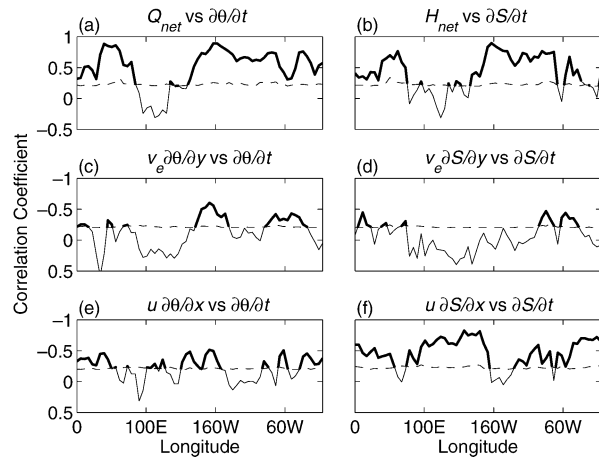


FIG. 13. Correlation coefficients of heat and salt storage rate ($\partial\theta/\partial t$, $\partial S/\partial t$) vs winter (a) net air–sea heat flux (Q_{net}), (b) net air–sea equivalent salt flux (H_{net}), (c) northward Ekman heat and (d) salt transports, and (e) zonal heat and (f) salt advection at the $\sigma_{27.2}$ outcrop latitudes. Note that the calculation is based on the first 100 yr of the model simulation, and is typical of the full 1000-yr run. Correlation is significant above the dashed line, which indicates a 95% significance level and is highlighted for clarity. Note that the advection terms require negative correlations to account for variability in the wintertime AAIW θ – S properties [refer also to Eqs. (1) and (2)]. Thus, for convenience, the correlation axes in (c)–(f) have been inverted so that the longitudes of significant correlation correspond to those regions above the dashed line.

zonal salinity gradients persist for longer in the ocean than zonal temperature gradients, because air–sea salt fluxes do not act to damp S anomalies in the same way air–sea heat fluxes damp θ anomalies.

To further understand the mechanisms controlling θ – S variability along the AAIW layer outcrop, we have calculated term correlation coefficients at each longitude over the first 100 yr of the model data. Significant positive correlation at zero lag between net winter surface heat flux and $\partial\theta/\partial t$ is found over much of the outcropping layer (Fig. 13a). The positive correlation implies increasing sea-to-air heat loss in winter corresponds with a higher temperature difference between late winter and late summer. That is, air–sea heat fluxes control the winter sea surface temperature variability. Significant positive correlation is also found at similar longitudes between the effective net surface salt flux and $\partial S/\partial t$ (Fig. 13b). This implies air–sea and/or ice–sea freshwater fluxes are controlling wintertime S variability at these locations.

In contrast to the surface flux correlations, northward Ekman transport of heat and salt shows only limited locations of significant correlation with the $\partial\theta/\partial t$, $\partial S/\partial t$ terms (Figs. 13c,d). For example, a significant correlation with heat storage rate holds in the South Pacific around 160°W and in the southeastern Atlantic near 40°–60°W. Both of these locations coincide with regions where the $\sigma_{27.2}$ outcrop is found farther away from the Antarctic coast (refer to Fig. 2). In other regions, where the outcrop layer is closer to the coast, northward Ekman

transport tends to be small in magnitude and gives little contribution to the variability in AASW heat content. Instead, atmospheric heat fluxes play the dominant role. Salinity variability due to northward Ekman transport is only significant in the southeast Pacific (near 80°–100°W) and in isolated locations of the South Atlantic and south Indian Oceans (Fig. 13d).

Analysis of correlations between $\partial\theta/\partial t$, $\partial S/\partial t$ and zonal advection at the $\sigma_{27.2}$ outcrop is shown in Figs. 13e and 13f. This reveals some locations where eastward propagation of anomalies is significantly in phase with θ – S trends. There is a tendency for this correlation to be high wherever surface flux and northward Ekman advection correlations are low, particularly for salinity (e.g., between 100° and 160°E). In these regions, ACC variability and/or variations in $\partial\theta/\partial x$ and $\partial S/\partial x$ play an important role in controlling surface water mass variability along $\sigma_{27.2}$. Note that near 100°E neither surface fluxes nor ocean advection are in phase with variability in θ – S . This suggests variability in mixing, most likely convective overturning, is controlling surface water mass variability in this region.

Because a variety of water types and densities contribute to AAIW, it is of some interest to assess variability mechanisms in other density classes. Most notably SAMW is known to contribute to AAIW ventilation (McCartney 1977), and while its variability has been studied elsewhere (Rintoul and England 2002), we briefly discuss here the mechanisms controlling θ – S anomalies along the outcrop of this lighter water mass ($\sigma_\theta \approx 26.9 \text{ kg m}^{-3}$). Meridional Ekman heat and salt transports play a more significant role in driving θ – S variability along the $\sigma_\theta = 26.9 \text{ kg m}^{-3}$ outcrop (refer to Tables 1 and 2). In particular, the northward Ekman transport now contributes almost as much variability as the surface flux terms. In addition, there are more regions of significant correlation between ocean advection and θ – S variations (figure not shown). Rintoul and England (2002) argue that SAMW variability is controlled by Ekman advection in both observations and a coupled model. However, we also find some SAMW regions in the CSIRO climate model where air–sea heat fluxes drive variability in $\partial\theta/\partial t$, notably in the South Pacific. In contrast to $\sigma_{27.2}$, though, ice–ocean coupling clearly plays no role at SAMW formation regions. In summary, in moving to lighter density classes than $\sigma_{27.2}$, Ekman advection plays a greater role in generating surface θ – S variability, while air–sea fluxes play a lesser role (and ice processes become negligible). For the rest of this paper we continue our focus on the $\sigma_{27.2}$ surface, namely, the AASW contribution to AAIW variability.

As noted previously, the mean position of the $\sigma_{27.2}$ outcrop layer exists at or just north of the absolute maximum sea-ice extent. That is, sea-ice frequency and concentration are generally low during the model 1000-yr simulation at $\sigma_{27.2}$ (refer to Figs. 14a,b). This suggests the $\sigma_{27.2}$ outcrop is normally exposed to the atmosphere, which means atmospheric heat and freshwater fluxes can

have a significant influence on the layer. Since the climate model includes sea-ice dynamics that allow the transport of sea ice by wind and ocean currents, the transport of ice also represents a transport of heat and salt (O’Farrell 1998). When ice is transported northward by the wind (or currents) at these latitudes, it melts and feeds in cold and fresh water to the intermediate water outcrop region, from where it will be mixed along isopycnals to intermediate depths. Figure 14c shows that the mean position of the outcrop lies within the region of negative ice-to-ocean salt flux, indicating meltwater input north of the sea-ice margin. Further analysis shows that anomalies in this meltwater rate are controlled, in part, by variations in the Ekman transport of ice to the north. Figure 15a shows the correlation between zonal winds versus ice-to-ocean fluxes over 100 yr of the model simulation. The band of negative correlations near 60°S corresponds to stronger westerly winds driving stronger meltwater rates. Thus, over much of the outcrop region, anomalous zonal wind can result in variations in ice–sea freshwater fluxes, which affect variability of S along $\sigma_{27.2}$.

The thin dashed lines in Fig. 14c show the northern and southernmost outcrop locations over the 1000-yr model run, implying that the $\sigma_{27.2}$ outcrop can lie within ice-free, ice-melting, and ice-forming regions (though it is not often in the latter). This geographic variability itself contributes to variability in surface heat and salt fluxes along the outcrop layer because these fluxes depend strongly on latitude. In addition, the mean outcrop layer is sometimes located over regions where sea-ice concentration variability is high; for example, in the southeast Pacific (Fig. 14d). This region corresponds to an area where θ – S variations are strongly controlled by anomalies in air–sea and ice–sea fluxes (Figs. 13a,b).

Last, note an important negative feedback mechanism that tends to stabilize the location of the $\sigma_{27.2}$ outcrop while also creating density-compensated θ – S anomalies in AASW. We have seen already that an increased zonal wind field induces sea ice melting (Fig. 15a). This meltback of ice means the surface water is more greatly exposed to increased latent and sensible heat fluxes (Fig. 15b). The meltwater dilution of surface salinity contributes to lighter AASW, which means a southward displacement of the outcrop layer (Fig. 15c). However, because of increased evaporative and sensible heat loss due to exposure of the ocean to cold air and wind, temperature decreases, leading to denser AASW (which is thus followed by a tendency for the outcrop layer to return northward, Fig. 15d).¹ This mechanism allows sea-ice variability to play a direct role in AASW θ – S variations by partly controlling thermohaline properties at the outcrop location.

¹ A net southward displacement of the isopycnal outcrop generally occurs with freshening despite cooling. This suggests that S has a larger effect on buoyancy than θ at the outcrop region.

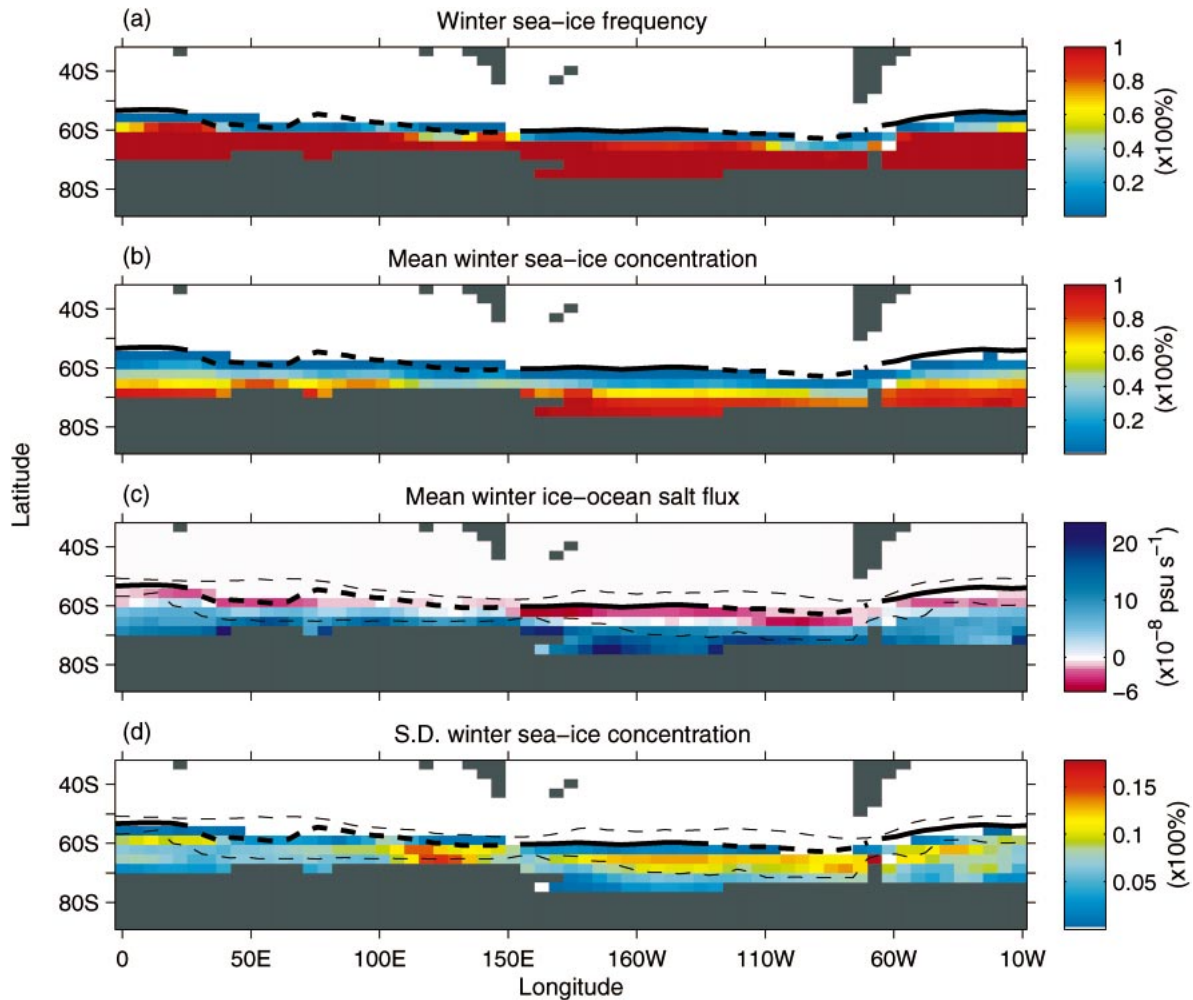


FIG. 14. Apr–Sep average of ice extent over 1000 yr showing (a) frequency of ice coverage, (b) mean ice concentration as a ratio of grid box area, (c) mean winter ice–ocean salt flux (H_{ice}), and (d) the standard deviation of the ice concentration. The mean location of the late-winter $\sigma_{27.2}$ outcrop is indicated by the solid line where the layer outcrop exists for the whole 1000 yr and by a dashed line otherwise. Thin dashed lines in (c) and (d) denote maximum and minimum displacement of the $\sigma_{27.2}$ outcrop ever attained over the 1000-yr model run (the southernmost extent excludes those years of no outcrop). North of 60°S in (c), sea-ice concentration is generally less than 60% and is marked by negative H_{ice} (freshwater input). Southward excursions of the $\sigma_{27.2}$ outcrop (i.e., low-density AASW) generally coincide with years of limited Antarctic sea ice.

6. Discussion and conclusions

The natural variability of AAIW θ – S properties and mechanisms is analyzed using a coarse-resolution climate model along the 1027.2 kg m^{−3} isopycnal surface ($\sigma_{27.2}$). This isopycnal surface coincides well with both the model and observed intermediate water salinity minimum (Fig. 1). The distribution of a passive tracer on the $\sigma_{27.2}$ surface suggests a mostly circumpolar formation of AAIW in the model with a substantial contribution from AASW (Fig. 3), as also seen in some other coarse-resolution models employing GM (e.g., Sørensen et al. 2001). Under this approach and based on the tendency of water properties to be mixed along isopycnals (e.g., Molinelli 1981), our study has focused on the AAIW variability sourced from AASW without taking

into account the contribution from SAMW (a lighter density class of AAIW).

The CSIRO climate model performs well in simulating mean AAIW θ – S properties and circulation resembling the observed. This is most likely due to a more realistic mixing parameterization and an improved representation of sea-ice processes incorporated in the model as shown in other studies (e.g., Sørensen et al. 2001; Duffy et al. 2001; Saenko and Weaver 2001). The variability of θ – S properties on the $\sigma_{27.2}$ isopycnal surface is documented at various time scales showing anomalies propagating eastward within the ACC with decreasing magnitude as they subduct northward into the interior (see Fig. 8). The CEOF analyses decompose the variability into three dominant modes showing mainly east-

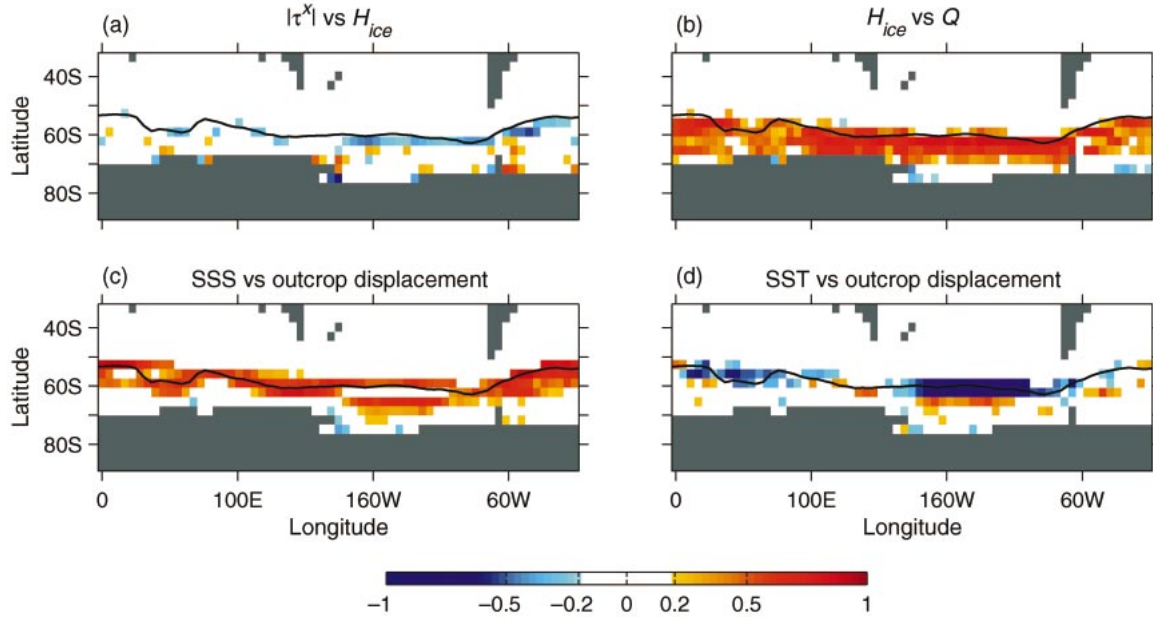


FIG. 15. Correlation maps for (a) winter zonal wind stress (τ^x) vs winter ice-ocean salt flux (H_{ice}), (b) winter H_{ice} vs winter surface heat flux (Q , which is dominated by outgoing heat fluxes), and (c) late-winter surface salinity and (d) late-winter surface temperature vs $\sigma_{27.2}$ outcrop displacement. Correlation coefficients are calculated using 100 yr of model simulation. The values are displayed when they are above the 95% significance level (refer to colorbar). The contour indicates the mean location of the late-winter $\sigma_{27.2}$ outcrop.

ward-propagating signals advected by the ACC (Fig. 9). The first mode shows a wavenumber-1 pattern consisting of signals at interannual to multidecadal time scales. Since the analysis is done on an isopycnal surface, isopycnal mixing most likely contributes to the low-frequency propagation (on centennial time scales). The high-frequency signals consist of subducted surface θ - S anomalies due mainly to variability in atmospheric heat fluxes and meltwater rates. The wavenumber-1 mode may also be in some way related to the Antarctic Dipole (ADP). Yuan and Martinson (2001) found the ADP to be a quasi-stationary wave existing as the dominant interannual variance structure in the sea-ice edge and surface air temperature fields in observations. The exact relation between the first AAIW mode in our study and the model's ADP requires further analysis and so is only speculative at this stage. The wavenumber-2 pattern of the second AAIW mode resembles the observed ACW, though showing a longer period than that described by White and Peterson (1996). A wavenumber-3 pattern is apparent in the third AAIW mode found in our CEOF analyses. This mode is analogous to that described by Cai et al. (1999), who employ a similar coupled model. The period of the wavenumber-3 AAIW mode in this study is mostly in the range 7–20 yr (see Fig. 10). The first three CEOFs of AAIW θ - S account for a total variability of about 53%. Higher CEOF modes (not shown), each accounting for a small fraction of total AAIW variability (<9%), exhibit eastward-propagating zonal wavenumber-4 and -5, and nonpropagating patterns.

A CEOF analysis on the SST field in the model's Southern Ocean between 33° and 62°S (not shown) is found to exhibit a zonal wavenumber-2 pattern with 8.9- and 20-yr periods, as well as a wavenumber-3 pattern with a dominant peak at 6.8-yr period. These patterns are similar to those found in AAIW CEOF modes 2 and 3, respectively. In addition, we also found variability in the sea-ice extent at 6.8- and 19.6-yr periods (figure not shown). This provides evidence of coherence between the spatial-temporal characteristics of variability at the surface and that in the interior at interannual to interdecadal time scales. The detection of ACW-like signals transmitted along the $\sigma_{27.2}$ surface from AASW into the interior suggests the role of AAIW in spreading climate signals to other parts of the globe.

In terms of comparison with recent observational studies of θ - S changes in AAIW, we found that the most extreme model cooling and freshening over 22–25 yr on the $\sigma_{27.2}$ surface is generally weaker than the observed (Bindoff and Church 1992; Johnson and Orsi 1997; Bindoff and McDougall 2000). This suggests the presence of a longer-term anthropogenic climate change signal in the observations.

The heat and salt budget analyses at the $\sigma_{27.2}$ outcrop region suggest salinity variability of AASW, (a major source of the model's AAIW), to be mainly due to sea-ice variability near the sea-ice margin (via meltwater). This is possible as the $\sigma_{27.2}$ isopycnal surface outcrops near the maximum sea-ice margin during winter in both the model and in the real ocean (Fig. 2). The temperature variability, on the other hand, is controlled mainly by

air–sea heat fluxes. We have found evidence that northward Ekman transport and zonal advection also play a significant but localized role in contributing to the variability. In the model Southern Ocean at 30°–60°S, changes in the late-winter sea surface temperature are generally accompanied by changes in sea surface salinity in a way that mostly conserves density (figure not shown; see also Rintoul and England 2002, their Fig. 6). Yet we find ice–ocean freshwater fluxes to control S , and air–sea heat fluxes to control θ . One possible way to achieve this would be for variations in the subpolar winds to control variations in the rate of sea-ice melting due to northward Ekman transport (Fig. 15a), which then controls the variation of evaporative and sensible heat loss (Fig. 15b). Under this scenario, an increased wind field drives ocean cooling and freshening via (respectively) air–sea and ice–ocean fluxes. Any variability in wind stress would also affect the strength of the ACC and thus affect variability at the outcrop region via zonal advection. Meridional Ekman advection would also be altered by the wind stress variations in such a way as to change θ and S in phase [this also dominates SAMW variability in Rintoul and England (2002)]. Thus, we expect wind stress variations to play a major role in AASW θ – S variability via any of these four mechanisms.

Last, we noted that heat and salt budget analyses on a lighter density class ($\sigma_\theta = 26.9 \text{ kg m}^{-3}$; see Tables 1 and 2), corresponding to SAMW, suggest a greater role for meridional Ekman advection in generating surface θ – S variability [consistent with Rintoul and England (2002)]. Air–sea heat fluxes play a lesser role and ice–ocean fluxes become negligible because the $\sigma_\theta = 26.9 \text{ kg m}^{-3}$ isopycnal outcrops substantially north of the sea-ice margin. However, as noted previously, SAMW appears to be a secondary contributor to AAIW renewal in this particular climate model, with subducted AASW playing the more dominant role.

Regardless of the AAIW formation mechanism, we find the water-mass properties along the core intermediate water layer to be largely controlled by variability in air–sea heat and freshwater fluxes, and sea-ice melt-water rates (with ocean advection playing a smaller role). Variations in these air–sea and ice–sea fluxes can introduce anomalies along the AAIW layer on time scales from years to decades.

Acknowledgments. This research is supported by the Australian Research Council and a University of New South Wales URSP grant. The authors gratefully acknowledge Mark Collier for preparing the model data output and Barrie Hunt for allowing us access to his 10 000-yr climate model simulations. We thank Peter Oke, Tony Hirst, and Steve Rintoul for helpful discussions, and acknowledge the constructive comments of two anonymous reviewers, which greatly improved the manuscript. Siobhan O’Farrell’s assistance in providing the tracer data is gratefully acknowledged. We also

thank Jo Jacka for the sea-ice data as made available online at <http://www.antcrc.utas.edu.au/~jacka/seaiice.html>.

REFERENCES

- Arbic, B. K., and W. B. Owens, 2001: Climatic warming of Atlantic Intermediate Waters. *J. Climate*, **14**, 4091–4108.
- Banks, H. T., R. A. Wood, J. M. Gregory, T. C. Johns, and G. S. Jones, 2000: Are observed decadal changes in intermediate water masses a signature of anthropogenic climate change? *Geophys. Res. Lett.*, **27**, 2961–2964.
- Barnett, T. P., 1983: Interaction of the monsoon and Pacific trade wind system at inter-annual time scales. Part I: The equatorial zone. *Mon. Wea. Rev.*, **111**, 756–773.
- Bindoff, N. L., and J. A. Church, 1992: Warming of the water column in the south-west Pacific. *Nature*, **357**, 59–62.
- , and T. J. McDougall, 1994: Diagnosing climate change and ocean ventilation using hydrographic data. *J. Phys. Oceanogr.*, **24**, 1137–1152.
- , and —, 2000: Decadal changes along an Indian Ocean section at 32°S and their interpretation. *J. Phys. Oceanogr.*, **30**, 1207–1221.
- Bonekamp, H., A. Sterl, and G. J. Komen, 1999: Interannual variability in the Southern Ocean from an ocean model forced by European Centre for Medium-Range Weather Forecasts reanalysis fluxes. *J. Geophys. Res.*, **104**, 13 317–13 331.
- Bryden, H. L., E. L. McDonagh, and B. A. King, 2003: Changes in ocean water mass properties: Oscillations or trends? *Science*, **300**, 2086–2088.
- Cai, W., P. G. Baines, and H. B. Gordon, 1999: Southern mid- to high-latitude variability, a zonal wavenumber-3 pattern, and the Antarctic Circumpolar Wave in the CSIRO coupled model. *J. Climate*, **12**, 3087–3104.
- Cox, M. D., 1984: A primitive equation, three-dimensional model of the ocean. GFDL Ocean Group Tech. Rep. No. 1, Princeton University, Princeton, NJ, 141 pp.
- Deacon, G. E. R., 1933: A general account of the hydrology of the South Atlantic Ocean. *Discovery Rep.*, **7**, 171–238.
- Duffy, P. B., and K. Caldeira, 1997: Sensitivity of simulated salinity in a three-dimensional ocean model to upper ocean transport of salt from sea-ice formation. *Geophys. Res. Lett.*, **24**, 1323–1326.
- , M. Eby, and A. J. Weaver, 1999: Effects of sinking of salt rejected during formation of sea ice on results of an ocean–atmosphere–sea ice climate model. *Geophys. Res. Lett.*, **26**, 1739–1742.
- , —, and —, 2001: Climate model simulations of effects of increased atmospheric CO₂ and loss of sea ice on ocean salinity and tracer uptake. *J. Climate*, **14**, 520–532.
- Emery, W. J., and R. E. Thomson, 1998: *Data Analysis Methods in Physical Oceanography*. Pergamon, 634 pp.
- England, M. H., 1992: On the formation of Antarctic Intermediate and Bottom Water in ocean general circulation models. *J. Phys. Oceanogr.*, **22**, 918–926.
- , 1993: Representing the global-scale water masses in ocean general circulation models. *J. Phys. Oceanogr.*, **23**, 1523–1552.
- , J. S. Godfrey, A. C. Hirst, and M. Tomczak, 1993: The mechanism for Antarctic Intermediate Water renewal in a World Ocean model. *J. Phys. Oceanogr.*, **23**, 1553–1560.
- Gent, P. R., and J. C. McWilliams, 1990: Isopycnal mixing in ocean circulation models. *J. Phys. Oceanogr.*, **20**, 150–155.
- Georgi, D. T., 1979: Modal properties of Antarctic Intermediate Water in the southeast Pacific and the South Atlantic. *J. Phys. Oceanogr.*, **9**, 456–468.
- Gordon, A. L., R. F. Weiss, W. M. Smethie, and M. J. Warner, 1992: Thermocline and Intermediate Water communication between the South Atlantic and Indian Oceans. *J. Geophys. Res.*, **97**, 7223–7240.
- Gordon, H. B., and S. P. O’Farrell, 1997: Transient climate change

- in the CSIRO coupled climate model with dynamical sea ice. *Mon. Wea. Rev.*, **125**, 875–907.
- Hirst, A. C., and T. J. McDougall, 1996: Deep-water properties and surface buoyancy flux as simulated by a z -coordinate model including eddy-induced advection. *J. Phys. Oceanogr.*, **26**, 1320–1343.
- , S. P. O'Farrell, and H. B. Gordon, 2000: Comparison of a coupled ocean–atmosphere model with and without oceanic eddy-induced advection. Part I: Ocean spinup and control integrations. *J. Climate*, **13**, 139–163.
- Horel, J. D., 1984: Complex principal component analysis: Theory and examples. *J. Climate Appl. Meteor.*, **23**, 1660–1673.
- Johnson, G. C., and A. H. Orsi, 1997: Southwest Pacific Ocean water-mass changes between 1968/69 and 1990/91. *J. Climate*, **10**, 306–316.
- Large, W. G., G. Danabasoglu, S. C. Doney, and J. C. McWilliams, 1997: Sensitivity to surface forcing and boundary layer mixing in a global ocean model: Annual-mean climatology. *J. Phys. Oceanogr.*, **27**, 2418–2447.
- Levitus, S., and T. Boyer, 1994: *Temperature*. Vol. 4, *World Ocean Atlas 1994*, NOAA ATLAS NESDIS 4, 117 pp.
- , R. Burgett, and T. P. Boyer, 1994: *Salinity*. Vol. 3, *World Ocean Atlas 1994*, NOAA ATLAS NESDIS 3, 99 pp.
- Mann, M. E., and J. M. Lees, 1996: Robust estimation of background noise and signal detection in climatic time series. *Climatic Change*, **33**, 409–445.
- McCartney, M. S., 1977: Subantarctic Mode Water. *A Voyage of Discovery: George Deacon 70th Anniversary Volume* (Suppl. to *Deep-Sea Res.*), M. V. Angel, Ed., Pergamon, 103–119.
- Mizoguchi, K., S. D. Meyers, S. Basu, and J. J. O'Brien, 1999: Multi- and quasi-decadal variations of sea surface temperature in the North Atlantic. *J. Phys. Oceanogr.*, **29**, 3133–3144.
- Molinelli, E. J., 1981: The Antarctic influence on Antarctic Intermediate Water. *J. Mar. Res.*, **39**, 267–293.
- O'Farrell, S. P., 1998: Sensitivity study of a dynamical sea ice model: The effect of the external stresses and land boundary conditions on ice thickness distribution. *J. Geophys. Res.*, **103**, 15 751–15 782.
- , 2002: Use of passive tracers as a diagnostic tool in coupled model simulations—Northern Hemisphere. *J. Phys. Oceanogr.*, **32**, 831–850.
- Percival, D. B., and A. T. Walden, 1993: *Spectral Analysis for Physical Applications*. Cambridge University Press, 583 pp.
- Pickard, G. L., and W. J. Emery, 1990: *Descriptive Physical Oceanography*. Butterworth Heinemann, 320 pp.
- Piola, A. R., and D. T. Georgi, 1982: Circumpolar properties of Antarctic Intermediate Water and Subantarctic Mode Water. *Deep-Sea Res.*, **29**, 687–711.
- , and A. L. Gordon, 1989: Intermediate water in the southwestern South Atlantic. *Deep-Sea Res.*, **36**, 1–16.
- Putman, W. M., D. M. Legler, and J. J. O'Brien, 2000: Interannual variability of synthesized FSU and NCEP–NCAR reanalysis pseudostress products over the Pacific Ocean. *J. Climate*, **13**, 3003–3016.
- Redi, M. H., 1982: Oceanic isopycnal mixing by coordinate rotation. *J. Phys. Oceanogr.*, **12**, 1154–1158.
- Rintoul, S. R., and S. Sokolov, 2001: Baroclinic transport variability of the Antarctic Circumpolar Current south of Australia (WOCE repeat section SR3). *J. Geophys. Res.*, **106**, 2795–2814.
- , and M. H. England, 2002: Ekman transport dominates local air–sea fluxes in driving variability of Subantarctic Mode Water. *J. Phys. Oceanogr.*, **32**, 1308–1320.
- Saenko, O. A., and A. J. Weaver, 2001: Importance of wind-driven sea ice motion for the formation of Antarctic Intermediate Water in a global climate model. *Geophys. Res. Lett.*, **28**, 4147–4150.
- , —, and M. H. England, 2003: A region of enhanced northward Antarctic Intermediate Water transport in a coupled climate model. *J. Phys. Oceanogr.*, **33**, 1528–1535.
- Schmid, C., G. Siedler, and W. Zenk, 2000: Dynamics of Intermediate Water circulation in the subtropical South Atlantic. *J. Phys. Oceanogr.*, **30**, 3191–3211.
- Sloyan, B. M., and S. R. Rintoul, 2001: Circulation, renewal, and modification of Antarctic Mode and Intermediate Water. *J. Phys. Oceanogr.*, **31**, 1005–1030.
- Sokolov, S., and S. R. Rintoul, 2000: Circulation and water masses along WOCE section P11: Papua New Guinea to Tasmania. *J. Mar. Res.*, **58**, 223–268.
- Sørensen, J. V. T., J. Ribbe, and G. Shaffer, 2001: Antarctic Intermediate Water mass formation in ocean general circulation models. *J. Phys. Oceanogr.*, **31**, 3295–3311.
- Storch, H. V., and F. W. Zwiers, 1999: *Statistical Analysis in Climate Research*. Cambridge University Press, 484 pp.
- Sverdrup, H. U., M. W. Johnson, and R. H. Fleming, 1942: *The Oceans: Their Physics, Chemistry, and General Biology*. Prentice Hall, 1087 pp.
- Talley, L. D., 1996: Antarctic Intermediate Water in the South Atlantic. *The South Atlantic: Present and Past Circulation*, G. Wefer et al., Eds., Springer Verlag, 219–238.
- White, W. B., and R. G. Peterson, 1996: An Antarctic circumpolar wave in surface pressure, wind, temperature and sea-ice extent. *Nature*, **380**, 699–702.
- Wong, A. P. S., N. L. Bindoff, and J. Church, 1999: Large-scale freshening of intermediate waters in the Pacific and Indian Oceans. *Nature*, **400**, 440–443.
- , —, and —, 2001: Freshwater and heat changes in the North and South Pacific Oceans between the 1960s and 1985–94. *J. Climate*, **14**, 1613–1633.
- Wüst, G., 1935: Schichtung und Zirkulation des Atlantischen Ozeans. Das Bodenwasser und die Stratosphäre. *Wiss. Ergeb. Dt. Atl. Exp. METEOR*, **6**, 1–288.
- Yuan, X., and D. G. Martinson, 2001: The Antarctic dipole and its predictability. *Geophys. Res. Lett.*, **28**, 3609–3612.